BAUDER
bilimsel araştırmalar
ve uygulamalar
derneği

AINTELIA SCIENCE NOTES

ISSN: 2822-4450

2026
Volume: 5
Issue : 1

www.bauder.org.tr

AIntelia Sciences Notes
Volume 5, Issue 1
June , 2026

Editor
M. Cem ALDAĞ
Bandırma Onyedi Eylül University
Bandırma, Balıkesir, Turkey

Publisher's Note

The articles included in this issue of the Aintelia Science Notes Journal (ASNJ) originate from the 1st International R&D, Design and Innovation Conference (REDin '26), held on May 15–16, 2026, at the BEBKA Konferans Salonu / Bursa, and organized under the auspices of BAUDER (Bilimsel Araştırmalar ve Uygulamalar Derneği). The papers presented here are the full conference texts submitted by the authors at REDin '26, published in this issue to ensure wider and lasting accessibility to the research community.

Table of Contents

Aintelia Science Notes

ASNJ • BAUDER PRESS

Research Article

Distinguishing Physical Stress Concentration from Numerical Singularity in Large-Scale Structural FEM Analyses

Samet Dönerkaya[1,*], Samet Büken[2]

1, 2 BVS R&D Center, Ankara, Türkiye

Correspondence to:
Samet Dönerkaya – s.donerkaya@bvs.com.tr

How to Cite:
Actual Citation as taken from website

RECEIVED: 17/03/2026
ACCEPTED: 01/04/2026
PUBLISHED: 30/06/2026

ABSTRACT

In large-scale structural finite element analyses (FEA), extreme stress peaks frequently occur at geometric discontinuities, boundary conditions, and perfectly bonded interfaces. These values are often directly compared with the material yield strength, which may lead to overly conservative or misleading safety assessments. However, such stress peaks may originate from mathematical singularities inherent to linear elastic formulations rather than physically admissible stress states. This study investigates the distinction between physical stress concentration and numerical singularity in an industrial-scale structural steel model subjected to end loading. A three-dimensional finite element model containing approximately one million elements was analyzed under service loading conditions. The simulation results indicated that the maximum von Mises stresses reached nearly three times the yield strength of S355JR steel. Through theoretical evaluation of asymptotic stress behavior, plastic deformation theory, mesh characteristics, and contact modeling effects, it is demonstrated that these stress peaks represent numerical artifacts rather than actual structural failure conditions. A systematic engineering interpretation framework is proposed to prevent the misclassification of singular stresses in industrial FEM applications.

KEYWORDS

Finite Element Analysis, Numerical Singularity, Stress Concentration, Structural Analysis, Welded Steel Structures

1. Introduction

Finite element analysis (FEA) has become the dominant validation tool in modern structural engineering applications. In large-scale industrial systems such as crane structures, welded steel assemblies, heavy machinery components, and load-bearing frames, numerical simulations frequently involve millions of degrees of freedom and are expected to provide direct quantitative indicators of structural safety. In common industrial practice, the maximum equivalent (von Mises) stress is directly compared with the material yield strength, and structural adequacy is evaluated according to this comparison. Although this approach is simple and practical, it implicitly assumes that the calculated stress field is physically meaningful throughout the entire computational domain.

However, this assumption is not valid in all situations. Linear elastic finite element formulations naturally admit stress fields that exhibit asymptotic behaviour near geometric discontinuities, boundary conditions, bonded interfaces, and idealized contact transitions. In such regions, stresses may theoretically increase without bound as the distance to the discontinuity approaches zero. Nevertheless, real materials cannot sustain infinite stresses, and therefore such behaviour cannot correspond to a physically admissible stress state.

The fundamental distinction between physical stress concentration and mathematical stress singularity is often not sufficiently addressed in routine industrial FEM applications. Physical stress concentrations arise from the redistribution of loads around geometric features such as holes, chamfers, notches, or weld toes. These stress increases are finite and exhibit convergent behaviour under mesh refinement. In contrast, singular stresses are theoretically unbounded and do not converge as the element size decreases. These stresses are numerical artefacts resulting from idealized boundary conditions, perfectly sharp geometries, and linear material modelling assumptions.

Misinterpreting singular stresses as actual structural overstress in large-scale industrial models may lead to serious engineering consequences. Such misinterpretations may result in unnecessary structural reinforcements, over-conservative design decisions, increased production costs, or incorrect failure predictions. Conversely, ignoring stress peaks without proper classification may lead to unsafe conclusions. Therefore, it is essential to establish a systematic framework capable of distinguishing physically meaningful stress concentrations from numerical singularities.

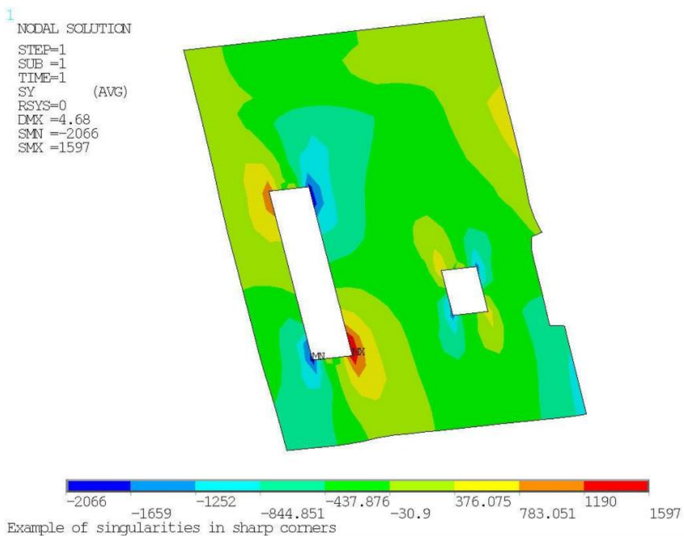

Figure 1: *Typical sources of stress singularities in finite element simulations, including sharp re-entrant corners and point loads.*

As illustrated in Figure 1, stress singularities may arise from several modelling idealizations frequently encountered in finite element simulations. Sharp geometric discontinuities, point load applications, and abrupt stiffness transitions introduced by boundary conditions may generate highly localized stress amplification. These modelling situations are particularly common in large industrial assemblies where complex connection regions and simplified boundary conditions are unavoidable. Therefore, distinguishing between physical stress concentration and mathematical stress singularity becomes a critical task in engineering interpretation.

Singularity problem becomes particularly critical in welded and contact-intensive steel assemblies. Perfectly bonded interfaces and idealized fixed supports introduce abrupt stiffness transitions that significantly amplify stress gradients. When combined with linear elastic material modelling, these conditions may produce calculated stress values that exceed the material yield strength even under service-level loading. Such results often raise serious concerns during industrial validation procedures; however, their physical relevance is not always critically examined.

Although stress singularities are well established in fracture mechanics and asymptotic elasticity theory, their interpretation within the context of large-scale industrial FEM analyses remains fragmented in the literature. Classical singularity theory is typically discussed in relation to crack tips and concave corners. In contrast, industrial analysts frequently encounter singular stress growth in crack-free structures, particularly near support edges and bonded contact interfaces. Bridging this gap between theoretical singularity concepts and practical large-scale simulation practice constitutes the primary motivation of this study.

In this work, a large-scale structural steel assembly subjected to end loading under linear elastic modelling is investigated. The numerical results show that the calculated von Mises stresses reach approximately three times the yield strength of S355JR steel. Instead of directly interpreting these stress peaks as indicators of structural failure, their numerical origin is analysed in terms of asymptotic stress behaviour, mesh dependency, material modelling limitations, and boundary condition idealizations. The objective of this study is not only to demonstrate the existence of singular stresses but also to develop a systematic engineering framework capable of distinguishing between finite physical stress concentration, mesh-dependent numerical stress growth, and actual structural overstress conditions. By clarifying this distinction, the reliability of structural interpretation in large-scale industrial FEM applications can be improved, thereby preventing both overly conservative and insufficient design decisions.

2. Literature Review

Stress singularities have been rigorously established within the framework of linear elasticity theory, particularly in the context of fracture mechanics and interface problems. The classical formulation developed by Rice (1968) demonstrated that the fields near crack tips in notched and cracked bodies can be characterized by path-independent integrals and asymptotically singular strain fields, thereby providing a physically meaningful measure of local stress concentration [1]. Subsequent asymptotic analyses expressed stress and displacement fields in terms of power-series expansions of the form r^λ, showing that the eigenvalues governing the order of singularity depend only on local geometry, boundary conditions, and material properties. In composite laminates and bimaterial interfaces, the order of the stress singularity is determined by the real part of the eigenvalue, and the interval $0 < \mathrm{Re}(\lambda) < 1$ represents physically admissible singular fields [2]. However, it must be emphasized that such singular solutions arise from the idealized assumptions of continuum elasticity. Real materials cannot sustain infinite stresses; therefore, singular behaviour must be interpreted as a mathematical consequence of the local boundary value problem. Nevertheless, asymptotically singular fields remain of central importance in fracture mechanics because they govern the fundamental quantities controlling crack initiation and propagation criteria. In this context, the characterization of singularity is physically meaningful and directly related to stress intensity factors.

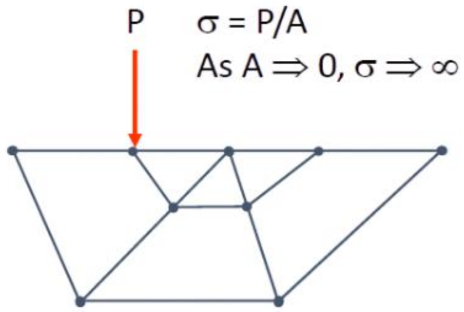

Figure 2: *Illustration of a stress singularity where the stress theoretically approaches infinity as the load application area tends toward zero.*

The mathematical origin of stress singularities can be understood through the relation between applied load and the effective load transfer area. As shown in Figure 2, when a force is applied over an infinitesimally small area, the theoretical stress tends to increase without bound as the area approaches zero. This behaviour represents a mathematical property of continuum mechanics formulations rather than a physically attainable stress state in real materials. Although singular solutions are analytically well understood, their numerical representation within classical finite element formulations involves significant challenges. It has long been recognized that quasi-uniform finite element meshes cannot accurately reproduce the stress field in the vicinity of a singular point [3]. To overcome this limitation, two principal approaches have been developed: local mesh refinement and basis function enrichment. Classical singular elements, such as quarter-point elements, enable accurate representation of stress fields of the form r^λ by embedding known asymptotic forms into the element interpolation. More recent developments combine the finite element method with the scaled boundary finite element method (SBFEM) through semi-analytical enrichment techniques, allowing the automatic treatment of singular behaviour without prior specification of asymptotic exponents [3–6]. These developments show that singularity handling is an active research area within computational mechanics. However, the majority of these studies focus on physically meaningful singular fields such as those found at crack tips. Comparatively few investigations have addressed singular stresses that arise unintentionally in large-scale industrial models because of geometric idealizations, discontinuous boundary conditions, or bonded interfaces.

In practical engineering applications, particularly in welded and large-scale steel assemblies, the interpretation of stress peaks is directly related to fatigue and strength assessment methodologies. Traditional finite element analyses generally use the maximum equivalent (von Mises) stress as a direct indicator of structural safety. However, such peak stresses are frequently mesh-dependent and may not represent a physically meaningful structural demand. Dong (2001) proposed a structural stress definition that separates stresses into membrane and bending components and remains insensitive to mesh size in the fatigue assessment of welded joints [7]. This approach clearly reveals the critical distinction between local stress concentrations and structural stress measures associated with damage mechanisms. In this context, it becomes evident that raw peak stresses extracted directly from finite element nodes near geometric discontinuities may be misleading. Similarly, stress singularities associated with traction discontinuities or line-supported stress distributions have been investigated using Airy stress function formulations [8]. These studies emphasize that stress intensifications observed along an interface or edge may be the consequence of idealized boundary conditions rather than actual structural overstress. More recent numerical studies involving singular source terms in elastic wave equations have likewise shown that the existence of mathematical singularities in the governing equations does not necessarily imply instability or physical collapse, provided that the global solution remains well defined and energetically bounded [9]. Classical fracture mechanics primarily focuses on square-root singularities of the form r^(−1/2). However, not all singular behaviour in elasticity takes the form of a pure power law. Under certain interface and boundary formulations, logarithmic stress singularities may arise. Sinclair and Epps (2002) showed that the use of displacement shape functions in submodelling boundary conditions can generate artificial logarithmic stress singularities because of derivative discontinuities in the prescribed displacement field [10]. Their analysis demonstrates that piecewise polynomial interpolation may produce spurious stress growth near boundary nodes even in otherwise regular elastic problems. This finding is particularly important for large-scale industrial finite element workflows in which global–local modelling or submodelling strategies are commonly employed. More recently, enriched crack-tip elements have been developed to explicitly represent logarithmic singular behaviour in interface fracture problems. Herrera-Garrido et al. (2026) proposed a special enriched element capable of reproducing logarithmic stress terms associated with spring-type interface models [11]. Their study confirms that logarithmic singularities can severely disrupt convergence behaviour in classical finite element formulations and that solution accuracy is significantly reduced if enrichment is not introduced. These studies clearly demonstrate that not all stress intensifications conform to classical crack-tip asymptotics. In industrial assemblies containing bonded interfaces, high-stiffness supports, or Robin-type boundary conditions, logarithmic-type stress growth may arise numerically even in the absence of a physical fracture process. Stress singularities are therefore not limited to cracks and V-notches.

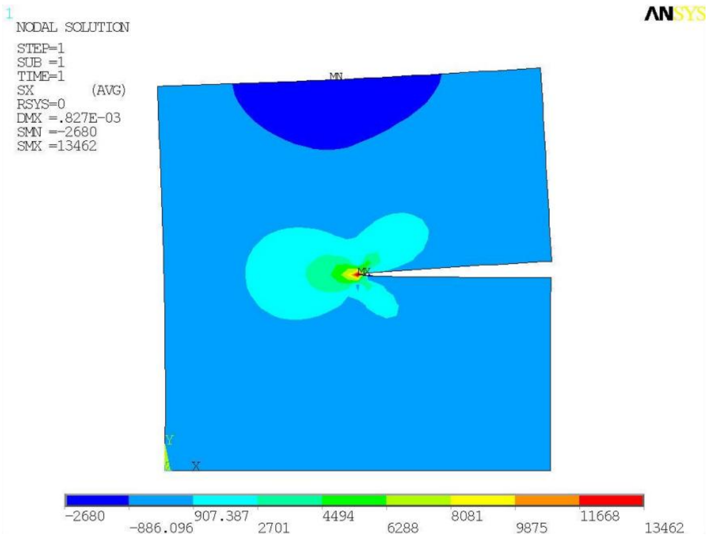

Figure 3: *Example of a classical stress singularity occurring at a crack tip predicted by linear elastic fracture mechanics.*

Contact mechanics problems also frequently exhibit singular stress behaviour, especially in stick–slip transition regions and at contact edges. Yue and Abdel Wahab (2014) investigated stress singularities arising in fretting contact under partial slip and gross sliding conditions [12]. Their finite element-based studies showed that singular stress signatures depend strongly on the fretting regime and the coefficient of friction. In particular, singular behaviour appears in high-friction partial-slip regimes, whereas it disappears under gross sliding conditions. This observation is of critical importance for industrial finite element applications. In large-scale steel assemblies, stress growth near bonded or frictional interfaces may represent regime-dependent singular fields rather than actual structural overstress. The eigenfunction expansion method has been widely used to determine the order of singular stresses in V-notched structures. Ping et al. (2008) developed a super-singular wedge-tip element containing numerical eigensolutions for anisotropic multi-material wedge tips [13]. This approach enabled rapid convergence in reproducing singular stress fields based on eigenvalue–eigenvector pairs. Similarly, Pageau et al. (1995) formulated a finite element approach for anisotropic materials exhibiting singular in-plane stress fields [14]. Their work extended eigenvalue analysis techniques to complex multimaterial junction regions and confirmed the dependence of singularity order on geometry and material properties. More recently, Pan et al. (2023) emphasized that the full stress field near a V-notch consists of both singular and higher-order non-singular terms [15]. These higher-order non-singular contributions were shown to have a significant influence on fracture prediction and stress intensity evaluation. The distinction between singular and non-singular contributions is therefore fundamental for interpreting peak stresses observed in numerical models. Collectively, these studies show that the order of singularity depends on local geometry and material mismatch, that higher-order non-singular terms influence practical stress assessment, and that accurate numerical extraction requires asymptotic consistency. However, these investigations mainly focus on the accurate solution of physically meaningful singular fields and do not provide a general framework for distinguishing numerical artefacts from physical stress concentrations in large-scale industrial assemblies.

A classical example of such behaviour is observed in the vicinity of crack tips, where the stress field follows an asymptotic power-law distribution. As illustrated in Figure 3, the stress theoretically increases as the distance to the crack tip decreases. While this formulation provides a physically meaningful framework in fracture mechanics, similar singular stress growth may also appear unintentionally in numerical simulations of crack-free structures due to modelling idealizations. Fatigue assessment methods for welded and large steel structures have sought to reduce the influence of mesh-dependent peak stresses. The structural hot-spot stress method (Poutiainen et al., 2004) provides extrapolation-based procedures for obtaining mesh-independent structural stress parameters [16]. Likewise, the Peak Stress Method (Visentini et al., 2022) accounts for singular peak behaviour while estimating notch stress intensity factors from coarse meshes [17]. These approaches acknowledge a critical fact: raw peak stresses obtained directly from finite element nodes near sharp weld toes or rigid supports are not always physically meaningful. Instead, fatigue-relevant structural stresses are obtained through extrapolation, energy-based averaging, or decomposition into membrane and bending components. Thus, the literature implicitly recognizes the risk of misinterpreting singular stress peaks; however, it still lacks a general framework capable of systematically distinguishing asymptotic physical stress concentration, numerical singular growth, and modelling-induced artificial stress amplification in large-scale linear elastic industrial models. Singularity theory has also been explored outside structural mechanics. Lei and Sornette (2025) proposed log-periodic power-law finite-time singularities in the prediction of rockbursts [18]. Although developed in a geomechanical context, this study reinforces an important conceptual point: mathematical singular behaviour does not automatically imply physical collapse; its interpretation must be made within the framework of energy admissibility and constitutive constraints. In classical elasticity, stress singularities have been systematically characterized through asymptotic eigenfunction analysis. Williams (1952) showed that stress behaviour at angular corners depends critically on the combination of boundary conditions and that certain corner angles subjected to mixed boundary conditions, such as clamped–free edges, may produce unbounded stresses [19]. This fundamental study established the eigenvalue-based characterization of singularity strength in angular regions. Building on Williams' formulation, Sinclair's comprehensive studies clarified the necessity of recognizing singular behaviour as well as strategies for its removal, interpretation, and asymptotic identification [20,21]. These works classified singularities into power-law, logarithmic, log-squared, and oscillatory forms, and emphasized that singular stresses are not physically realizable stress states but mathematical consequences of boundary value problems. Sinclair also noted that the onset of plasticity does not eliminate the singularity in the mathematical sense, because an elastic response must first develop prior to yielding [21]. This distinction is particularly important for large-scale industrial finite element models in which linear elastic formulations are widely used even when local peak stresses exceed the yield strength. Subsequent analytical studies extended singularity characterization to various notch geometries and loading modes. Semi-analytical boundary element approaches developed for V-notches demonstrated that stress intensity factors and higher-order asymptotic coefficients can be extracted directly from expansion amplitudes [22]. These approaches confirm that the order of singularity is governed by eigenvalue solutions dependent on notch opening angle and material properties. Finite element analyses of more general configurations have shown that singular behaviour also persists under partial slip and high-friction contact conditions [12]. The strong dependence of singular stress signatures on stick–slip transitions in fretting regimes indicates that contact constraints may give rise to singular-like numerical growth even in the absence of a crack tip. Error-assessment strategies for singular elements have also been developed. Meshii and Watanabe proposed a stress intensity factor error index based on known analytical displacement fields [23]. Their findings showed that singular field extraction is highly sensitive to mesh size and loading configuration, and that convergence analysis is essential for the interpretation of peak stresses. In practical fatigue assessment, several local stress and energy concepts have been developed to reduce mesh dependency and singular amplification. The local strain energy density (SED) approach, comprehensively reviewed by Radaj [24], is based on the average energy density within a finite control volume around the notch tip rather than on pointwise peak stress evaluation. This approach explicitly acknowledges that even if stresses are asymptotically singular, the averaged energy density may remain finite and physically meaningful. Similarly, the Peak Stress Method (PSM) provides a practical engineering solution by relating coarse-mesh peak stresses in welded joints to notch stress intensity factors [25]. This method accepts the existence of singular peak behaviour but transforms it into fatigue-relevant equivalent stress measures. In this way, an important conceptual shift occurs: the focus moves from interpreting absolute peak stress values to extracting physically interpretable parameters such as SIF, NSIF, SED, and structural stress.

In the present study, the persistent industrial gap between computed peak stresses and physically admissible stress states is addressed, and a structured interpretation workflow is developed and demonstrated for singular stress growth arising in large-scale structural finite element models. This workflow is based on the comparative evaluation of an industrial-scale structural assembly made of S355JR steel, analysed under service loading with gravity and consisting of approximately 2,027,936 nodes and 990,617 elements, and two representative simulations in which the model predicts highly localized von Mises peaks (680.952 MPa and 825.487 MPa), while the global displacements remain within the service range (for example, 6.60265 mm under end loading). Building upon established singularity-management approaches, the study explicitly tests and documents the influence of modelling idealizations, including point loads, fixed supports, and bonded/contact transitions, and applies corrective strategies such as replacing point forces with equivalent pressure loads, adding radii to re-entrant corners, and substituting fixed supports with contact-based boundary representations. To ensure that the observed stress growth is not incorrectly attributed to discretization artefacts, the work also includes mesh-quality assessments using standard metrics such as aspect ratio, skewness, Jacobian ratio, and related mesh diagnostic measures. Finally, in order to relate numerical peaks to physical admissibility, the interpretation is framed in terms of the fundamental principles of rate-independent plasticity, including the yield criterion, flow rule, and hardening rule, which are regarded as the natural regularization mechanisms for unbounded elastic stresses. Taken together, these steps provide a repeatable engineering methodology for distinguishing among (a) finite physical stress concentration, (b) mesh-dependent numerical singularity, and (c) actual structural overstress in large-scale industrial finite element applications.

3. Methodology

3.1. Numerical Model Description

The structural model analyzed in this study corresponds to an industrially designed crane girder assembly. The geometry was obtained in CAD format and subsequently prepared for finite element analysis in the ANSYS Mechanical 2025 R1 environment. The model represents the typical geometric and connection characteristics of large-scale steel structural systems. Prior to the analysis, a geometry preparation stage was conducted in which the solid model was converted into a surface model in order to reduce solution time and improve mesh quality.

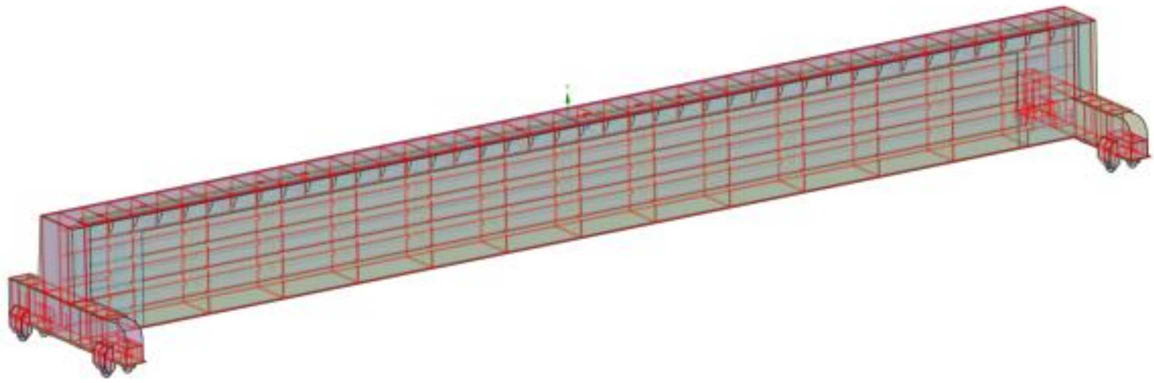

Figure 4: *Industrial crane girder assembly representing a typical welded structural system used in large-scale FEM simulations.*

The industrial crane girder assembly illustrated in Figure 4 was selected as the benchmark model for the present investigation. This structure contains several geometric discontinuities, connection interfaces, and load transfer regions typical of welded steel assemblies. Such characteristics make it a representative industrial case for examining the occurrence of stress singularities in large-scale finite element analyses. The selected crane girder assembly represents a realistic industrial-scale welded steel structure containing multiple geometric discontinuities, support interfaces and load transfer regions. Such configurations are known to produce strong stress gradients in finite element simulations and therefore constitute an appropriate benchmark for investigating numerical stress singularities. This transformation was performed in the ANSYS SpaceClaim environment using the midsurface command. Through the midsurface approach, thin-walled structural components were reduced to shell representations, allowing the generation of a more regular mesh structure while significantly reducing computational cost. This method increases solution efficiency while accurately representing the global stiffness behavior, particularly in long and thin-walled steel girder systems. During the model preparation phase, small geometric features that do not significantly influence the structural behavior, such as small radius, chamfers, and secondary holes, were removed from the geometry. This simplification process reduces unnecessary local mesh refinement, minimizes element distortion, and improves numerical stability. This step is particularly important for preventing artificial stress concentrations that may arise from sharp corners or small geometric details. In welded joint regions, a shared topology approach was applied in order to reduce the number of contact definitions and optimize computational performance. With this method, instead of defining separate contact interactions on adjacent surfaces, shared nodes are created between connected parts, thereby minimizing the need for bonded contact definitions. The use of shared topology improves the conditioning of the global stiffness matrix and significantly reduces solution time by eliminating unnecessary contact iterations. Across the model, eight fixed (clamped) boundary conditions were defined, and surface-based bonded contact interactions were used where necessary.

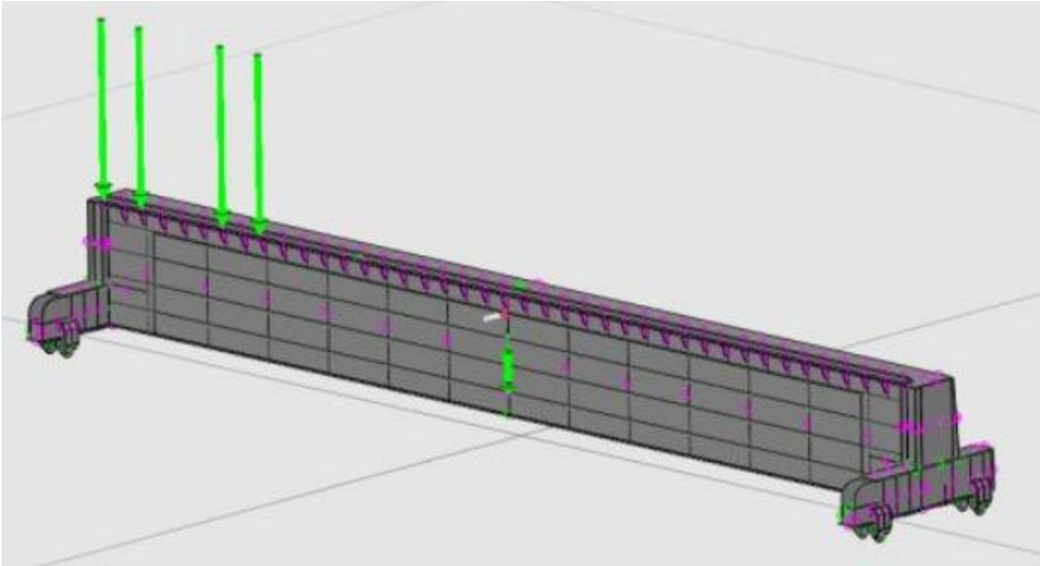

Figure 5: *Boundary conditions applied to the proposed CAD model.*

The boundary conditions applied to the model are shown in Figure 5. Although these constraints represent typical structural mounting conditions in industrial systems, they also introduce abrupt stiffness transitions within the numerical model. Under linear elastic assumptions, such transitions may significantly amplify local stress gradients, particularly near constrained edges and connection regions. These idealized boundary conditions were selected to represent the global load-bearing behavior of the structure. However, it is well known that fully clamped supports and bonded contact definitions may introduce abrupt stiffness transitions, which can lead to localized stress amplification under linear elastic analysis. Therefore, the modeling assumptions were selected deliberately with consideration for both computational efficiency and the interpretability of the resulting stress distribution. Consequently, the developed finite element model represents an industrial-scale steel assembly with a large number of degrees of freedom while preserving the global stiffness behavior of the system. This modelling framework provides a suitable basis for systematically investigating whether the stress peaks observed under linear elastic analysis originate from physically meaningful stress concentrations or from numerical singularities.

3.2. Material Model

In the analysis model, S355JR structural steel defined in the ANSYS material library was assigned to all structural components. The analyses performed within the scope of this study were conducted within the framework of a static linear structural solution, and the material behaviour was initially modelled as isotropic, homogeneous, and linear elastic.

Table 1: *Material card properties of S355JR steel.*

Properties of Outline Row 3: Structural Steel

	A	B	C	D	E
1	Property	Value	Unit		
2	Material Field Variables	Table			
3	Density	7850	kg m^-3		
4	Isotropic Secant Coefficient of Thermal Expansion				
5	Coefficient of Thermal Expansion	1.2E-05	C^-1		
6	Isotropic Elasticity				
7	Derive from	Young's M...			
8	Young's Modulus	2E+11	Pa		
9	Poisson's Ratio	0.3			
10	Bulk Modulus	1.6667E+11	Pa		
11	Shear Modulus	7.6923E+10	Pa		
12	Strain-Life Parameters				
13	Display Curve Type	Strain-Life			
14	Strength Coefficient	9.2E+08	Pa		
15	Strength Exponent	-0.106			
16	Ductility Coefficient	0.213			
17	Ductility Exponent	-0.47			
18	Cyclic Strength Coefficient	1E+09	Pa		
19	Cyclic Strain Hardening Exponent	0.2			
20	S-N Curve	Tabular			
21	Interpolation	Log-Log			
22	Scale	1			
23	Offset	0	Pa		
24	Tensile Yield Strength	2.5E+08	Pa		
25	Compressive Yield Strength	2.5E+08	Pa		
26	Tensile Ultimate Strength	4.6E+08	Pa		
27	Compressive Ultimate Strength	0	Pa		

In the linear elastic formulation, the material behavior is governed by Hooke's law:

$$\sigma = E\varepsilon \qquad (1)$$

where σ denotes the normal stress, E represents the Young's modulus of the material, and ε is the normal strain. Within this approach, the stress–strain relationship is linear, and the deformation remains fully recoverable as long as the stress level stays below the yield strength. Although the elastic solution is sufficient for examining the global stiffness behaviour of the structure, it does not physically limit local stress growths. S355JR steel is a ductile material, and once the yield strength is exceeded, plastic deformation begins. Plastic deformation occurs due to atomic slip along crystallographic planes caused by deviatoric stresses (dislocation motion), resulting in permanent strains. This behaviour is characterized by the inability of the material to return to its original configuration after the removal of the load.

3.3. Boundary Conditions and Loading

The boundary conditions and loading definitions applied in the numerical model were established in order to represent realistic industrial operating conditions of the crane girder assembly. In large-scale structural finite element analyses, the definition of appropriate boundary conditions plays a critical role in ensuring that the numerical model accurately reflects the physical load transfer mechanisms of the system. For this reason, boundary conditions and loading scenarios were carefully selected to represent the structural constraints and operational loading environment of the assembly. All analyses were performed within the framework of a static linear structural solution in ANSYS Mechanical. In this formulation, loads were applied in a single load step under the assumption of small deformations and linear material behaviour. This approach allows the global structural response to be evaluated efficiently while maintaining numerical stability and reducing computational cost. The loading configuration was defined in a manner consistent with typical service-level loading conditions encountered in industrial crane structures.

3.3.1. Support Conditions

In order to represent the mechanical connection between the crane girder assembly and the supporting chassis structure, fixed support (clamp) boundary conditions were assigned to eight hole regions located on the mounting interfaces of the model.

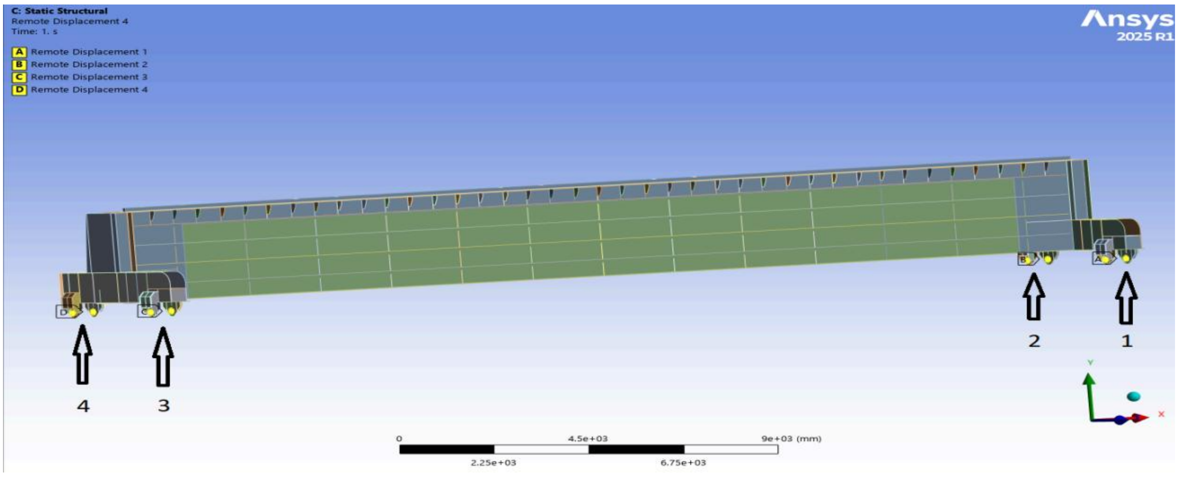

Figure 7: *Fixed support boundary conditions assigned to the hole regions of the CAD model.*

The fixed support locations illustrated in Figure 6 correspond to the mounting holes through which the structural assembly is attached to the supporting frame. While such boundary conditions are commonly used in structural simulations, they represent an idealization of the actual support stiffness and may therefore generate localized stress amplification in their vicinity. These hole regions correspond to the physical mounting points through which the structural assembly is connected to the supporting frame in the actual industrial system. By applying fixed support conditions at these locations, the structural constraints introduced by bolted or rigid mounting connections are represented in an idealized manner.

The fixed support definition constrains all translational displacement components at the associated nodes, such that

$$UX = UY = UZ = 0 \quad (2)$$

where UX, UY and UZ denote the translational displacement components in the global x, y and z directions, respectively. In other words, the nodes located on the support regions are prevented from undergoing any translational motion, effectively representing a rigid connection between the structure and its supporting base. This type of idealization is widely used in structural finite element modelling when the supporting structure is assumed to possess significantly higher stiffness than the analyzed component. Under such assumptions, the support structure can be considered rigid relative to the deformable structural assembly. However, it is also well established in the literature and in ANSYS technical documentation that fully fixed boundary conditions may introduce abrupt stiffness transitions within the numerical model. These transitions can result in steep stress gradients and local stress amplification, particularly in regions where constrained nodes interact with unconstrained structural domains. Such effects are especially pronounced in linear elastic analyses, where the absence of plastic deformation mechanisms prevents the redistribution of localized stresses. Consequently, high stress gradients and localized stress peaks are often observed near fixed support regions, particularly at geometric discontinuities or near support edges. For this reason, the interpretation of stress results in the vicinity of fixed supports must be performed with caution. In the context of the present study, these modelling assumptions were intentionally retained in order to allow the investigation of stress amplification behaviour and to distinguish between physically meaningful stress concentrations and numerical singularities arising from boundary condition idealizations.

3.3.2. Contact Definitions

In the numerical model, surface-based contact definitions were used for all interacting surfaces, and the contact type was assigned as bonded. Bonded contact prevents any relative displacement between contacting surfaces and enforces full displacement continuity at the corresponding nodes. This approach is commonly used for representing welded or rigid connections and provides a computationally efficient modelling strategy. However, bonded contact definitions may introduce abrupt deformation transitions, particularly between components with significantly different stiffness values. Under linear elastic analysis, such transitions may lead to localized stress amplification in the vicinity of the contact interfaces. In addition, through the application of the shared topology approach, common nodes were generated across many contact regions, thereby minimizing the number of explicit contact definitions required in the model. This modelling strategy reduces the number of contact solution iterations and improves computational efficiency. At the same time, it results in a mathematically fully connected structural system within the finite element model.

3.3.3. Loading Scenarios

In addition to the boundary conditions and contact idealizations described above, load definitions also represent important modelling parameters that may lead to stress singularities in linear elastic finite element models. In particular, point force applications or load definitions applied over vanishingly small areas may theoretically produce stress singularities under the continuum mechanics assumption. Two primary loading cases were considered in the numerical model. First, gravitational loading was applied to represent the self-weight of the structure. A gravitational acceleration of $-9.81\ m/s^2$ was imposed, and the load was introduced into the model as a distributed body force acting throughout the entire structural volume. Secondly, a service load was applied in the form of a concentrated force in order to represent operational loading conditions. A point force with a magnitude of 1.93×10^6 N was applied in the Z direction on the designated surface of the girder. The force components were defined as

$$FX = 0,\ FY = 0,\ FZ = 1.93 \times 10^6\ N \qquad (3)$$

Point force applications are known to represent boundary conditions that may theoretically generate singular behaviour within the framework of continuum mechanics. When a force is applied over an infinitesimally small area, the stress value tends to increase according to the relation $\sigma = P/A$ as the effective area approaches zero. For this reason, the interpretation of stress peaks obtained near the load application region requires careful physical evaluation.

3.3.4. Linear Static Solution Assumptions

All simulations performed within the scope of this study were conducted under a linear static structural analysis framework. Within this formulation, the geometry was assumed to remain unchanged during deformation and the material behaviour was defined as linear elastic. Accordingly, geometric nonlinearities such as large deflection effects were neglected, plastic material behaviour and yielding were not activated in the material model, and contact nonlinearities were simplified through the use of bonded contact definitions. Consequently, the structural response of the system was evaluated entirely within the framework of linear elasticity theory. While this modelling approach provides an efficient method for evaluating the global stiffness behaviour and load transfer characteristics of the structure, it does not impose any physical limitation on the growth of local stresses. In linear elastic finite element formulations, stress values may increase significantly in regions where abrupt stiffness transitions, geometric discontinuities, or highly concentrated loads are present. Such modelling assumptions may therefore lead to the appearance of numerical stress singularities, particularly near constrained boundaries, sharp geometric transitions, or point load applications. In these regions, stresses may theoretically approach very large values due to the absence of plastic deformation or geometric redistribution mechanisms that would otherwise limit stress growth. For this reason, the stress peaks observed in the analysis must be interpreted carefully. Rather than representing a physically meaningful stress state, these peaks may reflect mathematical singular behaviour introduced by the modelling assumptions. Therefore, the interpretation of the results focuses primarily on the overall stress distribution patterns and the stress values in neighbouring elements, where the numerical solution is less affected by singularity behaviour.

3.4. Singularity Identification and Classification Framework

Distinguishing whether high stress peaks obtained in large-scale linear elastic finite element analyses correspond to physical stress concentrations or numerical singularities constitutes the primary objective of this study. In order to address this issue, a systematic identification and classification strategy was developed to bridge the gap between the asymptotic singularity definitions reported in the literature and the practical interpretation challenges encountered in industrial finite element modelling applications.

3.4.1. Definition of Singularity and Numerical Indicators

According to ANSYS technical documentation, a stress singularity is characterized by the absence of stress convergence under mesh refinement, where the calculated stress values continue to increase as the mesh becomes progressively finer. From a mathematical perspective, this behaviour can be described through an asymptotic stress field expressed as

$$\sigma(r) \sim r^{(-\lambda)} \quad (4)$$

where r represents the distance from the singularity point and $\lambda > 0$ denotes the singularity order. As the distance approaches zero ($r \rightarrow 0$), the stress theoretically tends toward infinity.

However, such behaviour cannot occur in real engineering materials. In physical structures, mechanisms such as plastic deformation, microstructural damage, or geometric rounding limit the magnitude of stresses and prevent the formation of infinite stress values. For this reason, the identification of singularities cannot rely solely on the maximum stress magnitude obtained from numerical analysis. Instead, the characteristic behaviour of the stress field must be carefully examined in order to determine whether the observed stress amplification represents a physically meaningful stress concentration or a numerical artefact associated with singularity behaviour.

3.4.2. Identification Criteria

In this study, four evaluation criteria were used to classify the observed stress peaks. First, a mesh dependency analysis was conducted. The behaviour of the maximum stress values was examined as the mesh density increased in the suspected singularity regions. If the maximum stress continues to increase with mesh refinement without convergence, it indicates a high probability of numerical singularity; whereas converging stress values suggest a physical stress concentration. The mesh refinement results in this study showed that the stress peaks increased as the element size decreased, indicating non-convergent behaviour.

Secondly, a location analysis was performed by comparing the spatial positions of the suspected singularity regions with typical singularity sources reported in the literature, such as point loads, sharp re-entrant corners, fully fixed boundaries, and bonded contact transitions. In the analysed model, the highest stresses were concentrated around the clamped hole regions, bonded contact interfaces, and load application surfaces, indicating that the stress peaks are largely related to modelling idealizations.

Thirdly, the results were evaluated in terms of global structural behaviour. In a real overstress condition, global stiffness reduction, excessive displacement, or local instability would be expected. However, the analysis results showed maximum displacements of approximately 6.60 mm and 16.24 mm, and the structure behaved consistently with an elastic beam response.

Finally, a plastic admissibility assessment was performed. In linear elastic analysis, stresses may exceed the yield strength because yielding is not considered in the material model. In reality, S355JR steel begins to plastically deform once the yield strength is reached, and the stress state becomes limited by the yield surface. Therefore, the calculated elastic stress peaks in the range of 680–825 MPa cannot represent the real structural stress state and are expected to be physically limited by plastic yielding.

3.4.3. Classification Framework

Based on the criteria described above, the observed stress peaks were classified into three categories according to their numerical behaviour and physical interpretation. The classification was performed by analysing mesh dependency, spatial correspondence with typical singularity sources, compatibility with the global structural response, and the plastic admissibility of the calculated stresses. This framework enabled a systematic distinction between numerical singularities, physically meaningful stress concentrations, and elastically overestimated stresses that would be constrained by material yielding under real structural conditions.

According to this classification framework, the stress peaks observed in the analysed model were identified as Type 2, corresponding to mesh-dependent numerical singularities.

Table 2: *Stress classification framework.*

Category	Definition	Characteristic
Type 1	Physical stress concentration	Converges with mesh refinement
Type 2	Mesh-dependent numerical singularity	Increases with mesh refinement
Type 3	Actual structural overstress	Accompanied by deterioration in global structural behaviour

3.4.4. Engineering Mitigation Strategies

According to ANSYS technical documentation, if a stress singularity occurs within the region of interest of the analysis, several corrective modelling actions can be applied. Typical approaches include replacing point loads with equivalent pressure distributions, introducing fillets at sharp geometric corners, replacing fully fixed boundary conditions with more realistic contact interfaces, and evaluating averaged stress measures over finite control volumes rather than single-node peak values. These strategies are consistent with the singularity-management practices proposed by Sinclair [20,21] and with the mesh-independent structural stress and Peak Stress Method approaches developed for welded joints [7,16,25]. In the present study, mitigation was applied by combining geometric regularization at re-entrant corners with the substitution of fixed supports by contact-based boundary representations, thereby allowing the interpretation to focus on physically admissible stress fields rather than on isolated numerical extrema.

4. Results and Discussion

4.1. Asymptotic Stress Field Behaviour

Within the framework of linear elasticity theory, the stress field in the vicinity of geometric discontinuities and stiffness transition regions is commonly described by an asymptotic expression of the form:

$$\sigma(r) = K\, r^{(-\lambda)} \quad (5)$$

where r represents the distance from the singularity point and λ denotes the singularity order. When $\lambda > 0$, the stress theoretically tends toward infinity as $r \to 0$. This behaviour is not physical but arises from modelling assumptions and from the mathematical nature of the linear elastic solution.

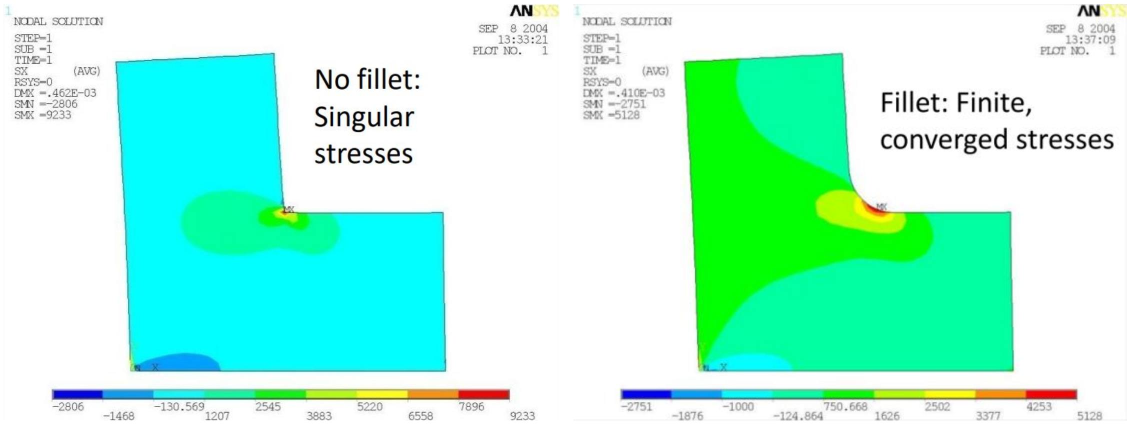

Figure 7: *Effect of geometric regularization on stress fields. Introducing a finite radius eliminates the stress singularity and produces convergent stresses.*

As demonstrated in Figure 7, geometric regularization plays a crucial role in the numerical behaviour of stress fields. Introducing a finite radius at sharp geometric transitions eliminates the mathematical singularity and results in convergent stress values. This observation highlights the fundamental difference between numerical singularities and physically meaningful stress concentrations. In the analyzed crane model, the maximum stress values were observed to concentrate in the hole regions where clamped boundary conditions were applied, at bonded contact transitions, and on the load application surfaces. All of these regions correspond to idealized modelling locations where abrupt stiffness variations occur. When mesh refinement was performed, the stress peaks did not converge and instead showed an increasing trend. This behaviour is consistent with the asymptotic growth predicted by classical singularity theory.

4.2. Energy-Based Interpretation

From a physical interpretation standpoint, the decisive factor in evaluating singularities is not only the magnitude of the stress but also the energy behaviour of the system. The elastic strain energy density is defined as

$$W = \tfrac{1}{2}\, \sigma_{ij}\, \varepsilon_{ij} \quad (6)$$

When the asymptotic stress expression is substituted into this formulation, the energy density varies approximately as $W(r) \sim r^{(-2\lambda)}$. The total elastic energy of the system can be expressed as the volume integral:

$$U = \int_V W\, dV \quad (7)$$

In cylindrical coordinates, this integral can be reduced to:

$$U \sim \int_0^{r_0} r^{(1-2\lambda)}\, dr \quad (8)$$

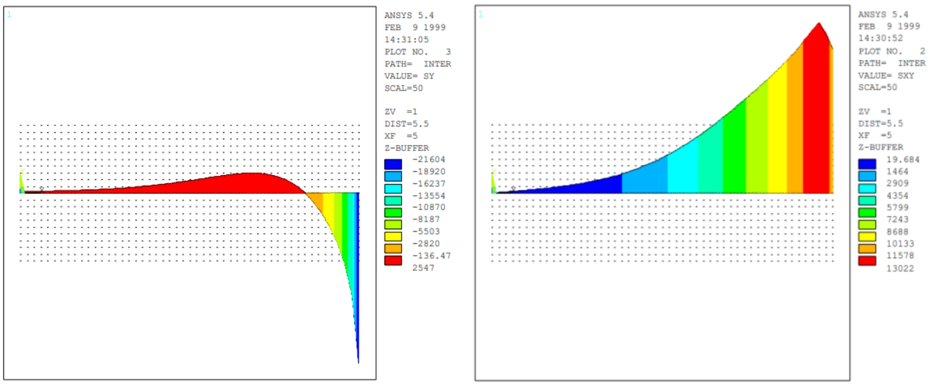

Figure 8: *Example of non-converging stress distributions near a singular region in finite element analysis.*

The stress distributions presented in Figure 8 clearly illustrate the non-converging behaviour typical of singular stress fields. As the evaluation point approaches the singular location, the stress magnitude increases rapidly rather than stabilizing at a finite value. Such behaviour indicates that the observed stress peak originates from asymptotic mathematical growth rather than from a physically distributed load transfer mechanism. For this integral to converge, the condition $\lambda < 1$ must be satisfied. In most structural singularities caused by boundary conditions, this condition is fulfilled. Under such circumstances, although the stress theoretically approaches infinity, the total strain energy remains finite. In the present analysis, the maximum displacement values were limited to 6.60 mm and 16.24 mm, indicating that the global energy balance of the system is preserved and that no loss of structural stiffness has occurred. This observation supports the mathematical nature of the singularity. While the stress field grows locally, the global structural response remains within physically acceptable limits.

4.3. Limits of the Elastic Solution and Plastic Regularization

In a linear elastic solution, the stress–strain relationship is defined by $\sigma = E\varepsilon$ (Eq. 1) and therefore does not include any yield limitation. As a result, the numerical model is mathematically capable of producing stress values exceeding the yield strength of the material. In real ductile steels, however, once the equivalent stress reaches the yield strength, plastic deformation begins and the stress field becomes limited by the yield surface. Plastic deformation acts as a natural regularization mechanism that prevents stresses from increasing indefinitely. For this reason, the stress peaks calculated in the linear elastic analysis, which lie in the range of 680–825 MPa, do not represent physically attainable stress states. These values arise from the mathematical growth permitted by the elastic formulation when plasticity is not included in the constitutive model.

4.4. Separation of Local and Global Structural Behaviour

In a real structural overstress condition, a reduction in global stiffness, uncontrolled growth in displacement, or a loss of structural stability would typically be expected. However, in the present study the global deformation behaviour of the system remained within serviceable limits. The energy integral remained finite and the overall load-carrying mechanism of the structure was preserved. Therefore, the observed stress peaks do not indicate actual structural failure but rather correspond to local asymptotic stress growth caused by modelling idealizations. The analyzed stress distribution can therefore be classified as a boundary-condition-induced numerical singularity rather than a physical stress concentration.

4.5. Implications for Industrial FEM Interpretation

These findings demonstrate that the maximum stress value alone cannot be used as a reliable safety indicator in large-scale linear elastic finite element analyses. In order to properly interpret stress peaks, the asymptotic behaviour of the stress field, the convergence characteristics of the energy response, and the plastic admissibility of the material must be evaluated together. Otherwise, purely mathematical singularities may be misinterpreted as structural failure, potentially leading to unnecessary design modifications and overly conservative engineering decisions.

5. Conclusions

5.1. Model Scale and Numerical Characteristics

The structure analyzed in this study corresponds to a large-scale industrial finite element model consisting of approximately one million elements. The model contains a total of 2,027,936 nodes and 990,617 second-order tetrahedral (TE10) elements. This numerical scale indicates that the solution possesses sufficient spatial resolution to represent the global structural behaviour rather than local numerical fluctuations. An evaluation of the mesh quality criteria shows that the majority of the elements fall within acceptable limits. Approximately 87.49% of the elements satisfy the aspect ratio criterion within the "good" quality range, with an average aspect ratio value of 3.056. The distributions of maximum and minimum element angles fall within acceptable limits for 96.68% and 95.18% of the elements, respectively. The average skewness value is 0.371, and 95.34% of the elements belong to the good-quality category. These mesh quality indicators demonstrate that the observed stress peaks are not caused by element distortion, excessive element deformation, or numerical instability. Therefore, the high stress values obtained in the analysis can be attributed to the nature of the boundary conditions and geometric discontinuities defined in the model rather than to poor mesh quality or numerical errors. Considering both the scale of the model and the adequacy of the mesh quality, the analysis results represent the behaviour of a realistic industrial structural system rather than that of simplified academic examples. This allows the stress singularity discussion presented in this study to be evaluated within a structural interpretation framework rather than as a consequence of numerical inadequacy.

5.2. Maximum Displacement and Global Structural Behaviour

As a result of the linear elastic analysis performed under service loading conditions, the maximum displacement of the structure was calculated as 6.60265 mm. The minimum displacement value is zero, which corresponds to the expected physical behaviour at the fixed support regions. Examination of the displacement distribution shows that the deformation exhibits a smooth and continuous bending profile along the girder. The maximum displacement occurs near the mid-span region, while the displacement magnitude gradually decreases toward the support regions. This distribution is consistent with classical bending theory for a beam subjected to end loading and indicates that the global stiffness behaviour of the structure is physically consistent.

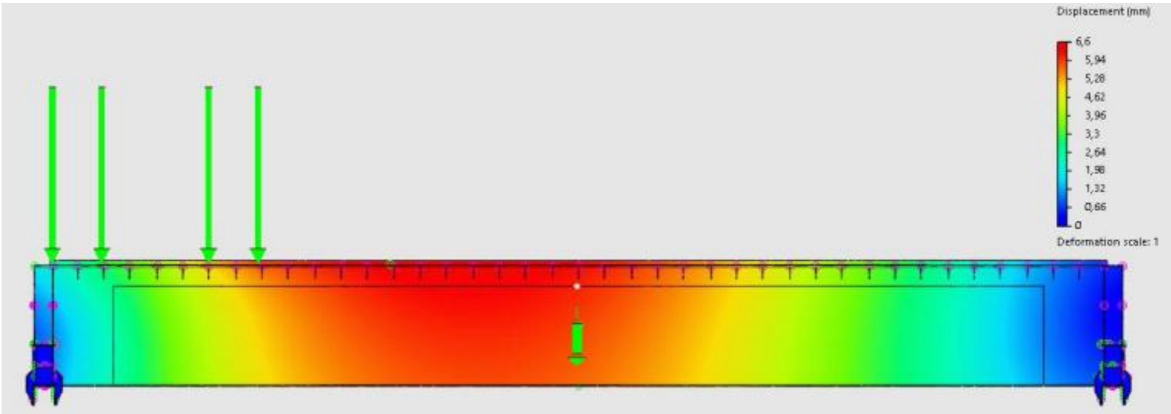

DOI: 10.5281/zenodo.21356417

Figure 12: *Displacement result of the crane beam under service loading conditions.*

Despite the presence of extremely high localized stress values, the global displacement field shown in Figure 9 exhibits a smooth and continuous deformation pattern. This behaviour is consistent with classical beam bending theory and indicates that the structural system retains its global stiffness under the applied loading conditions. This result plays a critical role in supporting the central argument of the present study. Although the maximum von Mises stress obtained in the same analysis reaches approximately three times the nominal yield strength of the material, the global deformation response of the structure remains limited and physically reasonable under service-level loading conditions. If the calculated high stress values represented a true structural overload condition, a significant loss of stiffness or a deviation from the linear elastic response would be expected in the global displacement behaviour of the system. However, no such anomaly is observed in the displacement field.

The continuity and smooth gradient of the displacement distribution also indicate that the numerical solution is stable. Despite the presence of very high stress values in the singularity regions, no discontinuities or irregular oscillations are observed in the displacement field. This suggests that the extreme stress values are concentrated within a very limited local region and do not control the global structural behaviour. In this context, the maximum displacement result serves as an important global performance indicator supporting the conclusion that the excessive stress values obtained in the analysis cannot be directly interpreted as indicators of structural failure. Since the deformation behaviour remains physically consistent, stable, and compatible with the expected bending mechanics under service loading, the local extreme stress values in the stress field should be evaluated within the framework of mathematical stress singularities.

5.3. Maximum von Mises Stress and Comparison with Yield Strength

The maximum equivalent (Von Mises) stress obtained from the analysis was calculated as 825.487 MPa. The material used in the model is S355JR structural steel, which has a 0.2% yield strength of 275 MPa. Accordingly, the calculated maximum stress value corresponds to approximately three times the yield strength:

$$\sigma_{max} / \sigma_y \approx 825 / 275 \approx 3 \qquad (9)$$

At first glance, this ratio may suggest that the structure is subjected to a severe overstress condition if the results of the linear elastic analysis are interpreted directly in terms of structural safety. However, a detailed examination of the stress distribution shows that this high value is concentrated within an extremely localized region. The majority of the global stress field remains within the range of 80–250 MPa, which lies within the yield strength limits of the material. The maximum stress values occur primarily in regions where rigid connections are modeled using bonded contact definitions and in areas containing sharp geometric discontinuities. In these regions, the stress field exhibits a very steep gradient, and the peak stress value is concentrated within a very small volume. Stress contour plots clearly indicate that the red high-stress region remains limited to the scale of individual elements, while the stress magnitude decreases rapidly in the surrounding elements. This behavior is consistent with the mathematical singularity characteristics described in classical elasticity theory. In the presence of sharp geometric corners or perfectly rigid boundary conditions, the stress field may increase asymptotically as the distance approaches zero. In contrast, if a real yielding condition were present, the stress increase would be expected to spread over a finite region through plastic deformation and would produce a measurable effect on the global stiffness of the structure. However, no such stiffness reduction is observed in the displacement field. Furthermore, since a linear elastic material model is used in the present analysis, the stress redistribution mechanism that occurs after yielding is not activated. In real material behavior, once plastic deformation begins, the stress field becomes limited and cannot increase indefinitely. Therefore, the 825 MPa value obtained in the elastic analysis does not represent a physically sustainable stress state but rather a numerical amplification resulting from the boundary conditions and geometric idealizations defined in the model. Consequently, the maximum von Mises stress value alone should not be interpreted as an indicator of structural inadequacy. When the localization of the stress field is evaluated together with the global deformation response, it becomes evident that the extreme stress values correspond to a mathematical singularity rather than to a physically meaningful overstress condition.

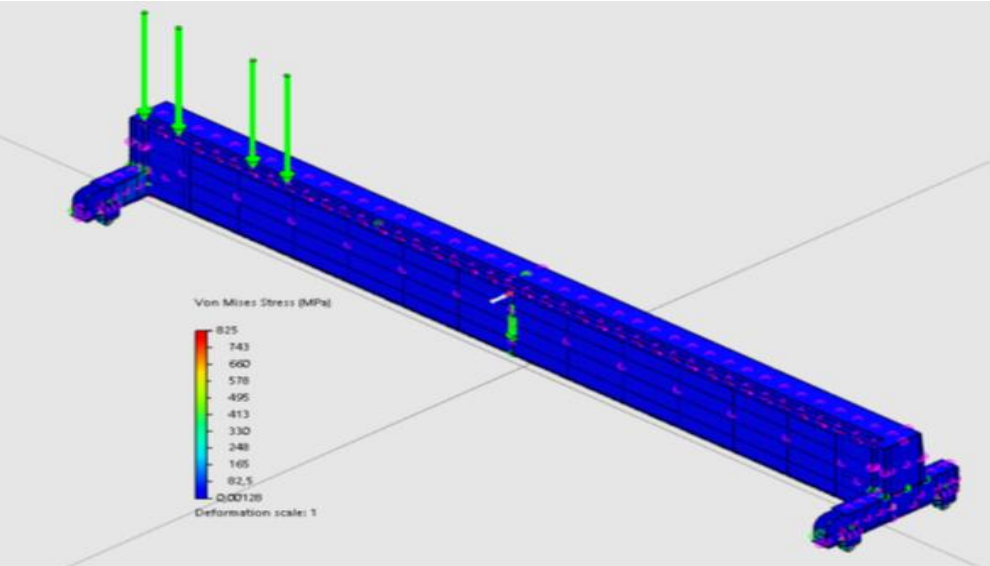

Figure 13: *Von Mises stress distribution of the crane beam.*

5.4. Mesh Quality and Numerical Reliability Assessment

The von Mises stress distribution illustrated in Figure 10 reveals that the extreme stress values are confined to a very limited region near geometric discontinuities and boundary interfaces. Outside these localized zones, the majority of the structure experiences stress levels well within the elastic range of the material. In order to technically support the singularity interpretation, it must first be demonstrated that the high stress values obtained in the analysis are not caused by poor mesh quality. For this reason, the mesh characteristics of the model were evaluated in detail. The finite element model used in the analysis consists of a total of 990,617 second-order tetrahedral (TE10) elements, and the element quality statistics were comprehensively examined. An evaluation of the mesh quality criteria shows that the majority of the elements fall within acceptable engineering limits. Approximately 87.49% of the elements satisfy the aspect ratio criterion within the "good" quality range, with an average aspect ratio value of 3.056. The maximum angle criterion falls within the acceptable range for 96.68% of the elements, with an average value of 105.802°. The minimum angle criterion is acceptable for 95.18% of the elements, with an average value of 29.439°. The average skewness value is 0.371, and 95.34% of the elements belong to the good-quality category. In terms of the stretch criterion, 87.81% of the elements also satisfy the good-quality range. These indicators demonstrate that the model does not contain element distortion, excessive element stretching, deteriorated angle distributions, or numerical instability related to element shape quality. In particular, the high percentage of elements classified as "good" in terms of skewness and minimum angle distribution indicates that the stress calculations are not significantly influenced by geometric discretization errors. An examination of the mesh structure in the regions where the stress peaks occur shows that the elements are not distorted or excessively elongated; instead, a homogeneous and numerically stable discretization is achieved. Therefore, the stress peaks reaching 825 MPa cannot be attributed to deficiencies in mesh quality but must instead be interpreted as physical stress concentrations or mathematical singular behaviour caused by boundary condition idealizations.

5.5. Overall Interpretation

Taken together, the model scale, mesh quality, global displacement behaviour, and localized peak stress magnitude collectively demonstrate that the high stress values observed in the analysis do not represent a real structural overstress condition but instead exhibit the characteristics of mathematical singularities. The study demonstrates, through a large-scale industrial model, the distinction between physical stress concentrations and numerical singularities, highlighting the importance of careful interpretation of finite element results in engineering practice. The proposed evaluation approach reduces the risk of unnecessary overdesign while also preventing incorrect safety assessments. In large-scale structural analyses, not only the magnitude of the stress field but also its behavioural characteristics and physical plausibility must be considered.

STATEMENTS AND DECLARATIONS

Supplementary Material

No supplementary material accompanies this article.

Acknowledgements

The authors gratefully acknowledge BVS R&D Center for providing the industrial CAD model, licensed software resources, and computational infrastructure used in this study.

Author Contributions

S. Dönerkaya: Conceptualization, Methodology, Formal Analysis, Investigation, Writing – Original Draft. S. Büken: Methodology, Software, Validation, Writing – Review & Editing.

Conflicts of Interest

The authors declare that they have no known competing financial interests or personal relationships that could have appeared to influence the work reported in this paper.

Data, Code & Protocol Availability

The data supporting the findings of this study are available from the corresponding author upon reasonable request. Model files remain the intellectual property of BVS R&D Center and are subject to the company's data-sharing policy.

Funding Received

This research did not receive any specific grant from funding agencies in the public, commercial, or not-for-profit sectors.

ORCID IDs

Samet Dönerkaya https://orcid.org/0000-0001-7577-5124
Samet Büken https://orcid.org/0009-0004-8824-5199

REFERENCES

1. J. R. Rice, "A path independent integral and the approximate analysis of strain concentration by notches and cracks," J. Appl. Mech., vol. 35, no. 2, pp. 379–386, 1968.
2. A. Carpinteri and M. Paggi, "Asymptotic analysis of stress singularities in composite laminates," Compos. Struct., vol. 71, pp. 210–219, 2005.
3. J. Bulling, H. Gravenkamp, and C. Birk, "A high-order finite element technique with automatic treatment of stress singularities by semi-analytical enrichment," Comput. Methods Appl. Mech. Eng., vol. 355, pp. 135–156, 2019, doi: 10.1016/j.cma.2019.06.013.
4. S. H. Ebrahimi, S. Mohammadi, and I. Mahmoudzadeh Kani, "A local PUFEM modeling of stress singularity in sliding contact with minimal enrichment for direct evaluation of generalized stress intensity factors," Eng. Fract. Mech., vol. 105, pp. 16–40, 2013.
5. Y. Qian and B. Teng, "A finite element–scaled boundary finite element coupled method for corner singularities in 2D second-order radiation problems," Ocean Eng., vol. 281, art. 114910, 2023, doi: 10.1016/j.oceaneng.2023.114910.
6. C. Wang, X. Ping, and X. Wang, "An adaptive finite element method for crack propagation based on a multifunctional super singular element," Int. J. Mech. Sci., vol. 247, art. 108191, 2023, doi: 10.1016/j.ijmecsci.2023.108191.
7. P. Dong, "A structural stress definition and numerical implementation for fatigue analysis of welded joints," Int. J. Fatigue, vol. 23, no. 10, pp. 865–876, 2001, doi: 10.1016/S0142-1123(01)00055-X.
8. A. Montanino and A. Iannuzzo, "A quadrilateral plate-type finite element to model stress singularities in no-tension materials," Comput. Methods Appl. Mech. Eng., vol. 432, art. 117433, 2024, doi: 10.1016/j.cma.2024.117433.
9. L. Jing, M. Feng, Y. Li, F. Teng, and Z. Luo, "A reduced-dimension method for unknown Crank–Nicolson finite element solution coefficient vectors of elastic wave equation with singular source term," J. Math. Anal. Appl., vol. 540, art. 128629, 2024, doi: 10.1016/j.jmaa.2024.128629.
10. G. B. Sinclair and B. P. Epps, "On the logarithmic stress singularities induced by the use of displacement shape functions in boundary conditions in submodelling," Commun. Numer. Methods Eng., vol. 18, pp. 121–130, 2002, doi: 10.1002/cnm.473.
11. M. A. Herrera-Garrido, L. Távara, M. Muñoz-Reja, A. Vázquez-Sánchez, and V. Mantič, "Enriched crack-tip element for logarithmic stress singularities of Mode I and II cracks in spring interfaces," Eng. Fract. Mech., vol. 336, art. 111941, 2026.
12. T. Yue and M. Abdel Wahab, "Finite element analysis of stress singularity in partial slip and gross sliding regimes in fretting wear," Wear, vol. 321, pp. 53–63, 2014, doi: 10.1016/j.wear.2014.09.008.
13. X.-C. Ping, M.-C. Chen, and J.-L. Xie, "Singular stress analyses of V-notched anisotropic plates based on a novel finite element method," Eng. Fract. Mech., vol. 75, pp. 3819–3838, 2008, doi: 10.1016/j.engfracmech.2008.01.003.
14. S. S. Pageau, P. F. Joseph, and S. B. Biggers Jr., "Finite element analysis of anisotropic materials with singular in-plane stress fields," Int. J. Solids Struct., vol. 32, no. 5, pp. 571–591, 1995, doi: 10.1016/0020-7683(94)00152-9.
15. W. Pan, C. Cheng, F. Wang, Z. Hu, and J. Li, "Determination of singular and higher order non-singular stress for angularly heterogeneous material notch," Eng. Fract. Mech., vol. 292, art. 109592, 2023, doi: 10.1016/j.engfracmech.2023.109592.
16. I. Poutiainen, P. Tanskanen, and G. Marquis, "Finite element methods for structural hot spot stress determination — a comparison of procedures," Int. J. Fatigue, vol. 26, pp. 1147–1157, 2004, doi: 10.1016/j.ijfatigue.2004.04.004.
17. A. Visentini, A. Campagnolo, V. Babini, and G. Meneghetti, "Automated implementation of the Peak Stress Method for the fatigue assessment of complex welded structures," Forces Mech., vol. 6, art. 100072, 2022, doi: 10.1016/j.finmec.2021.100072.
18. Q. Lei and D. Sornette, "Oscillatory finite-time singularities in rockbursts," Int. J. Rock Mech. Min. Sci., vol. 192, art. 106156, 2025, doi: 10.1016/j.ijrmms.2024.106156.
19. M. L. Williams, "Stress singularities resulting from various boundary conditions in angular corners of plates in extension," J. Appl. Mech., vol. 19, pp. 526–528, 1952, doi: 10.1115/1.4010550.
20. G. B. Sinclair, "Stress singularities in classical elasticity—I: Removal, interpretation, and analysis," Int. J. Numer. Methods Eng., vol. 60, no. 5, pp. 993–1018, 2004, doi: 10.1002/nme.1002.
21. G. B. Sinclair, "Stress singularities in classical elasticity—II: Asymptotic identification," Int. J. Numer. Methods Eng., vol. 60, no. 6, pp. 1019–1045, 2004, doi: 10.1002/nme.1003.

22. Y. Huang, C. Cheng, Z. Hu, D. Kondo, and R. Das, "Stress singularity analysis for the V-notch with a novel semi-analytical boundary element," Eng. Anal. Bound. Elem., vol. 163, pp. 84–93, 2024, doi: 10.1016/j.enganabound.2024.03.006.
23. T. Meshii and K. Watanabe, "Stress intensity factor error index for finite element analysis with singular elements," Eng. Fract. Mech., vol. 70, pp. 657–669, 2003, doi: 10.1016/S0013-7944(02)00083-9.
24. D. Radaj, "State-of-the-art review on the local strain energy density concept and its relation to the J-integral and peak stress method," Fatigue Fract. Eng. Mater. Struct., vol. 37, no. 10, pp. 1091–1112, 2014, doi: 10.1111/ffe.12231.
25. A. Visentini, A. Campagnolo, V. Babini, and G. Meneghetti, "Automated implementation of the Peak Stress Method for the fatigue assessment of complex welded structures," Forces Mech., vol. 6, art. 100072, 2022, doi: 10.1016/j.finmec.2021.100072.

Aintelia Science Notes

ASNJ • BAUDER PRESS

Research Article

The Harvest of Algorithms: A New Path from Data to Efficiency

Algoritmaların Hasadı: Veriden Verimliliğe Yeni Bir Yol

Ahmet Mermer[1,*]

1 Erkunt Traktör Sanayii A.Ş., Ankara, Türkiye

Correspondence to:
Ahmet Mermer – ahmetmrmr@gmail.com
+90 507 040 2434

How to Cite:
Actual Citation as taken from website

RECEIVED: 21/04/2026
ACCEPTED: 29/04/2026
PUBLISHED: 30/06/2026

ABSTRACT

In the modern agricultural landscape, digital transformation has evolved into a high-precision engineering discipline. This study analyzes advanced automated guidance systems as a decisive bridge between conventional mechanics and the era of autonomous farming. By integrating high-torque actuation with intelligent positioning logic, these systems utilize multi-constellation satellite networks and real-time correction streams to achieve a precision level where operational deviations are confined to the centimeter scale. This technological framework, synchronized via high-speed CAN-Bus communication and real-time data fusion, optimizes complex field trajectories for critical tasks such as seeding and precision fertilization. The synergy between advanced control units and intuitive human-machine interfaces minimizes the margin of human-induced error, leading to a significant reduction in fuel consumption and mechanical fatigue. Beyond basic navigation, features such as dynamic terrain compensation and automated headland path planning ensure consistent accuracy across diverse topographies. This research posits that the true "harvest" of these algorithms lies in the transition from manual control to data-driven operational intelligence. As a critical milestone toward fully unmanned agricultural ecosystems, these advanced positioning solutions provide a robust foundation for economic optimization and environmental stewardship, defining the next frontier of smart mechanization.

KEYWORDS

Automated Guidance, Data-Driven Agriculture, High-Precision Positioning, Operational Efficiency, Smart Mechanization

ÖZET
Modern tarım ekosisteminde dijital dönüşüm, artık basit bir otomasyon sürecinin ötesine geçerek yüksek hassasiyetli bir mühendislik disiplini hâline gelmiştir. Bu çalışma, gelişmiş otomatik yönlendirme sistemlerini, geleneksel mekanik yaklaşımlar ile otonom tarım çağı arasında belirleyici bir köprü olarak ele almakta ve analiz etmektedir. Yüksek torklu aktüasyon yapıları ile akıllı konumlandırma algoritmalarının entegrasyonu sayesinde bu sistemler; çoklu uydu takımyıldızları ve gerçek zamanlı düzeltme sinyallerinden faydalanarak, operasyonel sapmaların santimetre mertebesinde sınırlandığı bir hassasiyet düzeyine ulaşmaktadır. Yüksek hızlı CAN-Bus iletişimi ve gerçek zamanlı veri füzyonu ile senkronize edilen bu teknolojik altyapı, ekim ve hassas gübreleme gibi kritik tarla operasyonları için karmaşık hareket yollarını optimize etmektedir. Gelişmiş kontrol üniteleri ile sezgisel insan-makine arayüzleri arasındaki sinerji, operatör kaynaklı hata payını minimuma indirirken; yakıt tüketimi ve mekanik yorgunlukta kayda değer bir azalma sağlamaktadır. Temel yönlendirme işlevlerinin ötesinde, dinamik arazi telafisi ve otomatik başak (headland) dönüş planlaması gibi özellikler, farklı topografik koşullar altında dahi tutarlı konumsal hassasiyet sunmaktadır. Bu araştırma, algoritmaların gerçek "hasadının"; manuel kontrolden veriye dayalı operasyonel zekâya geçişte ortaya çıktığını ileri sürmektedir. Tam otonom tarımsal ekosistemlere geçiş yolunda kritik bir kilometre taşı niteliği taşıyan bu gelişmiş konumlandırma çözümleri, ekonomik optimizasyon ve çevresel sürdürülebilirlik için sağlam bir temel sunarak akıllı mekanizasyonun bir sonraki sınırını tanımlamaktadır.

Anahtar Kelimeler: Akıllı Mekanizasyon, Operasyonel Verimlilik, Otomatik Yönlendirme, Veriye Dayalı Tarım, Yüksek Hassasiyetli Konumlandırma

1. GİRİŞ

Artan üretim gereksinimleri ve sürdürülebilirlik beklentileri doğrultusunda tarım sektörü dijitalleşmeyi hızla benimsemektedir. Geleneksel manuel direksiyon çözümleri; operatör kaynaklı hatalara, yakıt israfına ve düşük doğruluk seviyelerine yol açarken, teknoloji odaklı çözümler bu zorlukları önemli ölçüde ortadan kaldırmaktadır. Bu yenilikler arasında otomatik dümenleme sistemleri, modern tarımın en kritik bileşenlerinden biri olarak öne çıkmaktadır. Traktörlerdeki konumlandırma ve yönlendirme süreçlerini dijitalleştiren bu sistemler; GNSS (Küresel Navigasyon Uydu Sistemi) tabanlı konumlama ve RTK (Gerçek Zamanlı Kinematik) düzeltme sinyallerinden faydalanarak yaklaşık ±2.5 cm hassasiyet seviyesine ulaşmakta ve ekim, gübreleme ve ilaçlama gibi operasyonlarda yüksek doğruluk sağlamaktadır (Şekil 1).

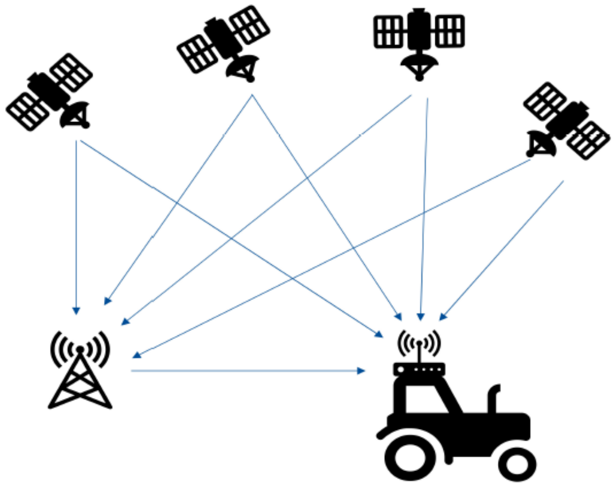

Şekil 1: *Sinyalin Çalışma Prensibi*

Otomatik dümenleme sistemleri; bir elektrik motoru, elektronik kontrol ünitesi (ECU), GNSS alıcısı ve sezgisel bir tablet arayüzünden oluşmaktadır. Bu bileşenler, CAN-Bus (Controller Area Network) protokolleri üzerinden haberleşerek gerçek zamanlı veri alışverişi ve sistemler arası sorunsuz entegrasyon sağlamaktadır. Direksiyon kolonuna monte edilen elektrik motoru, operatör müdahalesine gerek kalmadan otomatik yönlendirme görevini yerine getirirken; kullanıcı, tablet arayüzü üzerinden yol planlama, başak (headland) dönüş otomasyonu ve arazi telafisi gibi işlevleri kolaylıkla yönetebilmektedir.

Bu teknoloji, yalnızca yönlendirme hassasiyetini artırmakla kalmayıp; aynı zamanda iş gücü verimliliğini yükseltmekte, yakıt tüketimini optimize etmekte ve tarımsal operasyonlarda sürekliliği güvence altına almaktadır. Bununla birlikte, veriye dayalı yönetim anlayışı ve bağlantılı sistemler ile bütünleşmiş bir yapı sunarak, yakın gelecekte tam otonom tarım makinelerinin temel altyapısını oluşturması beklenmektedir. Özetle, otomatik dümenleme sistemleri; modern tarımda dijitalleşme ve sürdürülebilirlik hedeflerine ulaşılmasında stratejik bir rol üstlenmektedir.

Elektrik motoru tahrikli otomatik dümenleme sistemleri; mekanik olarak entegre edilmiş direksiyon kolonu yapıları ve optimize edilmiş tork iletimi sayesinde tarım araçlarında yüksek hassasiyetli yönlendirme performansı sunmaktadır [5] (Şekil 2).

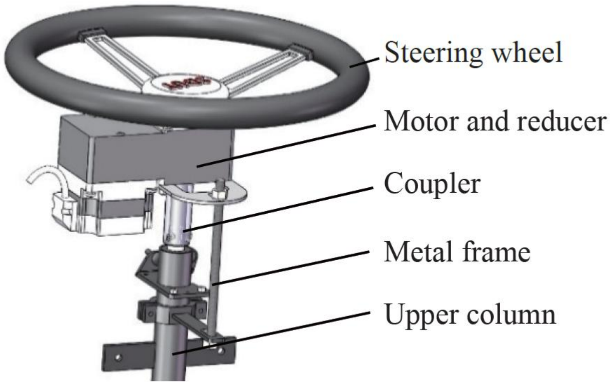

Şekil 2: *Direksiyon Mekanizmasının Montajı*

CAN-Bus tabanlı haberleşme mimarileri üzerinde çalışan gelişmiş kontrol algoritmaları; değişken yük koşulları altında dahi gerçek zamanlı tepki kabiliyeti ve sistem kararlılığı sağlamaktadır [5].

GNSS ağlarının RTK düzeltme sinyalleri ile desteklenmesi, farklı tarla koşulları altında santimetre seviyesinde konumlandırma hassasiyetinin korunmasını sağlarken; otomatik yönlendirme sistemlerinde sinyal sapmasını azaltmakta ve geçişten geçişe tekrarlanabilirliği önemli ölçüde iyileştirmektedir [6].

Tarım makinelerinde kullanılan CAN-Bus ağlarının güvenilirliği ve siber güvenliği, otomatik dümenleme sistemlerinin kesintisiz ve kararlı bir şekilde çalışmasının sağlanmasında kritik bir rol oynamaktadır. Makine öğrenmesi tabanlı anomali tespit yaklaşımları, olağandışı haberleşme desenlerini belirleyerek operasyonel güvenliği artırmakta ve sistem kaynaklı duruş sürelerinin azaltılmasına katkı sağlamaktadır [4] (Şekil 3).

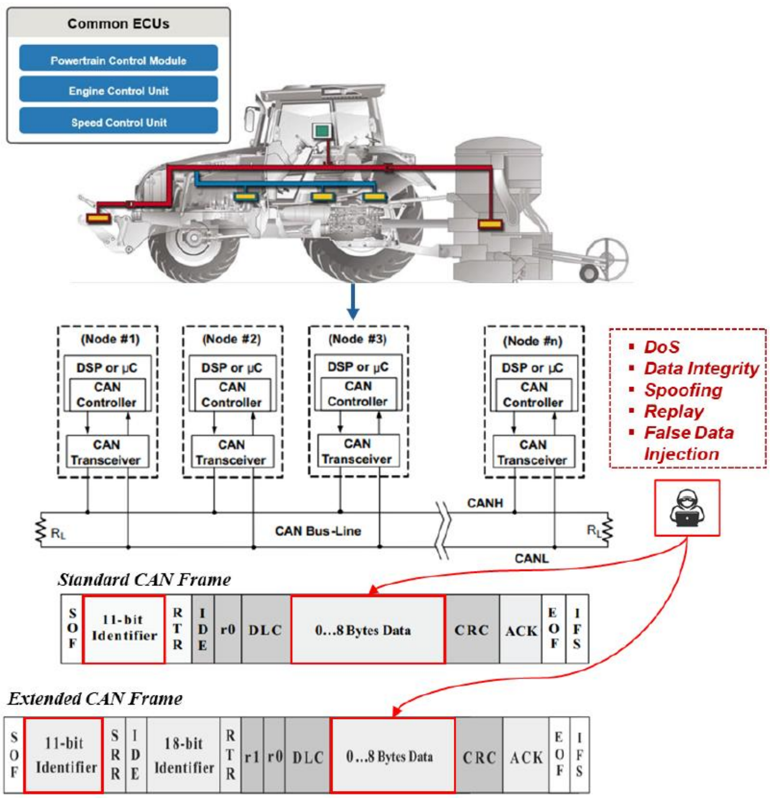

Şekil 3: *Modern Tarım Makinelerinde CAN Uygulaması ve Örnek Saldırı Vektörleri*

Otomatik dümenleme sistemleri, otonom tarım teknolojilerine geçiş sürecinde temel bir yapı taşı olarak değerlendirilmektedir. IoT platformları ve sensör füzyonu yaklaşımları ile entegrasyonun;

insansız tarla operasyonlarının yaygın biçimde benimsenmesi açısından önemli bir potansiyel sunduğu öngörülmektedir [2] (Şekil 4).

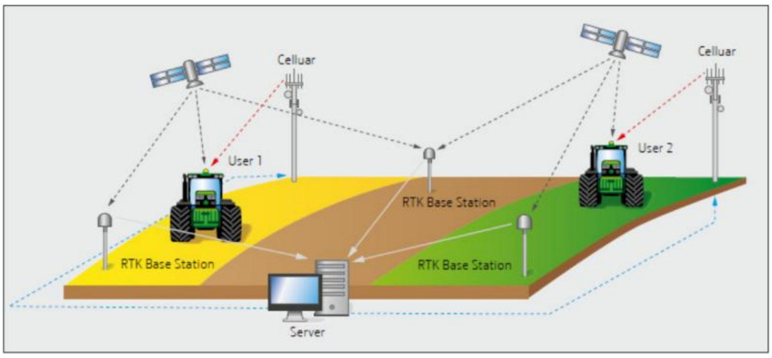

Şekil 4: *İnsansız Saha Operasyonları için IoT Platform Entegrasyonları*

GNSS tabanlı konumlandırma sistemlerinin RTK düzeltme sinyalleri ile entegrasyonu, otomatik dümenleme uygulamalarında santimetre seviyesinde konumsal hassasiyetin korunmasını mümkün kılmaktadır. Bu yaklaşım; sinyal sapmasını azaltmakta, geçişten geçişe tekrarlanabilirliği artırmakta ve özellikle hassas tarım uygulamalarında yönlendirme performansını önemli ölçüde iyileştirmektedir [3], [1].

2. Materyal ve Yöntem

2.1. Materyal

Bu çalışmada, traktörlerde kullanılan otomatik dümenleme sistemlerinin yapısı, temel bileşenleri ve performans parametreleri incelenmiştir. Sistem, GNSS (Küresel Navigasyon Uydu Sistemi) tabanlı konumlandırmanın RTK (Gerçek Zamanlı Kinematik) düzeltme sinyalleri ile entegrasyonu sayesinde hassas tarım uygulamalarında yüksek doğruluk sağlayacak şekilde tasarlanmıştır. GNSS alıcısı traktörün gerçek zamanlı konumunu belirlerken, RTK modülü santimetre seviyesinde konumsal düzeltmeler sunmaktadır. Geliştirilen otomatik dümenleme sistemi, saha değerlendirmeleri kapsamında Erkunt Nimet 75Lux Deutz-V traktör modeli üzerine başarıyla uygulanmıştır (Şekil 5).

Şekil 5: *Otomatik Direksiyon Sistemi*

Saha testleri süresince, navigasyon kontrolcüsü tarafından oluşturulan operasyonel komutlar otomatik aktüasyon mekanizmalarına iletilmiştir. Direksiyon kolonuna entegre edilen elektrik motoru, elektronik kontrol ünitesi (ECU) tarafından üretilen komutlar doğrultusunda yönlendirme hareketlerini gerçekleştirmiştir. Operatör ise yol planlama, başak (headland) dönüş otomasyonu ve arazi telafisi gibi fonksiyonları tablet tabanlı bir kullanıcı arayüzü üzerinden yönetmiştir.

Konum Belirleme ve Hassasiyet (R70 GNSS Alıcısı)

Traktörün konumunun yüksek hassasiyetle belirlenebilmesi amacıyla sistem, GNSS (Küresel Navigasyon Uydu Sistemi) alıcıları aracılığıyla uydu sinyallerini toplamaktadır (Şekil 6). Elde edilen bu sinyaller, RTK (Gerçek Zamanlı Kinematik) düzeltme teknolojisi kullanılarak işlenmekte ve ±2.5 cm doğruluk seviyesine ulaşılmaktadır. RTK düzeltmeleri, GNSS sinyallerini bir referans istasyonundan alınan verilerle senkronize ederek, hatasız yol planlaması ve sıra takibini güvence altına almaktadır.

Şekil 6: *R70 GNSS Alıcısının Traktör Üzerindeki Konumu*

Veri İşleme ve Kontrol (Direksiyon ECU)

Konumlandırma verilerinin işlenmesi ve yönlendirme komutlarının üretilmesi amacıyla Elektronik Kontrol Ünitesi (ECU), GNSS ve RTK verilerini almakta; gelişmiş algoritmalar kullanarak traktörün mevcut konumunu ve hedef güzergâhını hesaplamakta ve buna bağlı olarak direksiyon açı komutlarını oluşturmaktadır (Şekil 7). Sistem bileşenleri arasındaki haberleşme ise CAN-Bus (Controller Area Network) protokolü üzerinden yönetilmektedir.

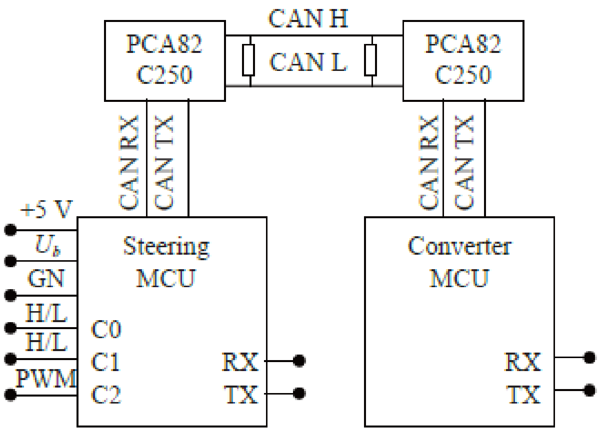

Şekil 7: *Elektronik Kontrol Ünitesi (ECU) Blok Şeması*

Direksiyon Otomasyonu (EMS2 Motoru)

Operatör müdahalesi olmaksızın yönlendirme işlemini gerçekleştirmek amacıyla, direksiyon kolonuna entegre edilen yüksek torklu bir elektrik motoru, ECU tarafından üretilen komutlara bağlı olarak direksiyon açısını ayarlamakta ve bu sayede traktörün önceden tanımlanmış güzergâhları otomatik takip etmesini sağlamaktadır (Şekil 8).

Şekil 8: *Direksiyon Mekanizmasının Montajı*

Kullanıcı Arayüzü ve İşlev Yönetimi (T100 Monitör)

Operatöre sezgisel kontrol ve izleme imkânı sağlamak amacıyla, tablet tabanlı arayüz üzerinden yol planlama, başak (headland) dönüş otomasyonu, arazi telafisi ve hız ayarı gibi fonksiyonlar yönetilmektedir (Şekil 9). Kullanıcı arayüzü; gerçek zamanlı konum bilgilerini, sistem durumunu ve performans metriklerini görsel olarak sunmaktadır.

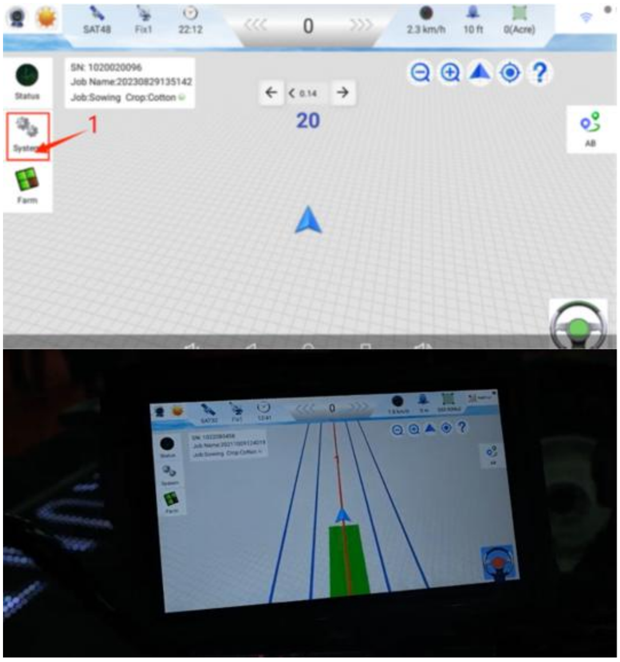

Şekil 9: *Sezgisel Kontrol Mekanizması (T100 Monitör Arayüzü)*

2.2. Yöntem

Bu aşamada, otomatik dümenleme sisteminin performansı ISO 12188-2 standartlarına uygun olarak saha koşulları altında değerlendirilmiştir. Deney süresince, lastik ölçüleri ve lastik basınç değerleri, ETRTO 2018 standartları doğrultusunda sabit tutulmuş ve test koşullarının tekrarlanabilirliği sağlanmıştır (Tablo 1).

Tablo 1: *Lastik Bilgileri*		
	Lastik Boyutu	**Lastik Basıncı (bar)**
Ön Lastikler	280/85R24	1.6
Arka Lastikler	420/85R30	1.6

Deneyler, sert asfalt zemin üzerinde gerçekleştirilmiş ve üç farklı zaman aralığında tekrarlanmıştır. İlk test, sistemin montajı ve kalibrasyonunun hemen ardından uygulanmıştır. İkinci test, ilk testten bir saat sonra, üçüncü test ise yirmi dört saat sonra gerçekleştirilmiştir. Her bir test oturumu sırasında çevresel koşullar izlenmiş ve kayıt altına alınmıştır (Tablo 2).

Tablo 2: *Deney Esnasında Hava Koşulları*			
Deneyler	**Hava Sıcaklığı °C**	**Nem (%)**	**Hava Durumu**
I. Başlangıç	30°C	31%	Açık
II. 1 Saat	28°C	40%	Parçalı Bulutlu
III. 24 Saat	20°C	65%	Şiddetli Yağmur

Testlere başlamadan önce, tüm yazılım ayarları ve kullanıcı tarafından yapılandırılabilen parametreler varsayılan değerlerine sıfırlanmıştır. Araç parametreleri hassas şekilde ölçülerek sisteme girilmiş ve seçilen çalışma moduna uygun olarak kalibrasyon prosedürleri uygulanmıştır. Kalibrasyonun ardından, A–B referans hattı boyunca yapılan gidiş ve dönüş geçişleri arasındaki mesafe farkı ölçülerek ince ayarlamalar gerçekleştirilmiş ve bu fark ofset değeri olarak tanımlanmıştır. Söz konusu ayarlar, tüm test süreci boyunca değiştirilmeden korunmuştur (Şekil 10).

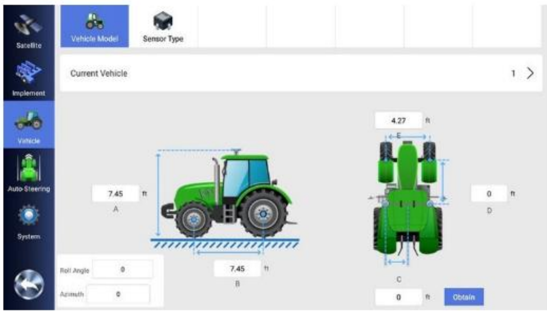

Şekil 10: *Araç Ayarları Ekranı*

Veri boşluklarının, test sonuçlarının geçerliliğini etkilemeyecek düzeyde (<%25) olduğu belirlenmiştir. Konum Hassasiyeti Zayıflama Faktörü (Position Dilution of Precision – PDOP) değerlendirmesi kapsamında, aktif uydu sayısı 31, potansiyel uydu sayısı ise 32 olarak kaydedilmiştir. Saha çalışmalarında kullanılan uydu konumlandırma cihazı tarafından gözlemlenebilen maksimum uydu sayısı 34 olarak belirlenmiştir. Tüm deneyler süresince seyir hızı ve motor devri sabit tutulmuştur. Traktör, tüm test senaryolarında 2.5 m/s seyir hızı ve 1400 d/d (rpm) motor devrinde çalıştırılmıştır (Tablo 3).

Tablo 3: *Test Parametreleri*		
Deneyler	**Seyir Hızı (m/s)**	**Motor Devri (dev/dk)**
I. Başlangıç	2.5 m/s	1400 rpm
II. 1 Saat	2.5 m/s	1400 rpm
III. 24 Saat	2.5 m/s	1400 rpm

3. Bulgular

Bu kapsamda, otomatik dümenleme sistemi (ODS) testleri 2.5 m/s sabit seyir hızı altında ve tüm operasyon süresince operatör müdahalesi olmaksızın gerçekleştirilmiştir. Seçilen hız ayarı için her bir test, farklı GNSS (Küresel Navigasyon Uydu Sistemi) uydu takımyıldızı konfigürasyonları altında, iki ardışık gün boyunca ve üçer tekrar şeklinde uygulanmıştır (Şekil 11).

Şekil 11: *Test Rotası*

Bu yaklaşım, farklı uydu geometrileri altında sistem performansının değerlendirilmesine olanak sağlamıştır.

3.1. İlk Test Sonuçları

Birinci test kapsamında, otomatik dümenleme sisteminin (ODS) ileri ve geri geçişler sırasında elde edilen GNSS istatistikleri kaydedilmiştir. Elde edilen veriler, her bir geçiş için ayrı ayrı değerlendirilmiş ve grafiksel olarak sunulmuştur (Şekil 12 ve Şekil 13).

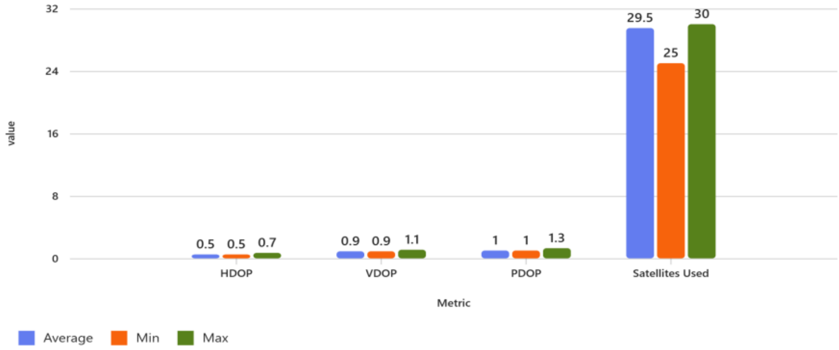

Şekil 12: *Birinci Test Gidiş Yönü GNSS Değerleri*

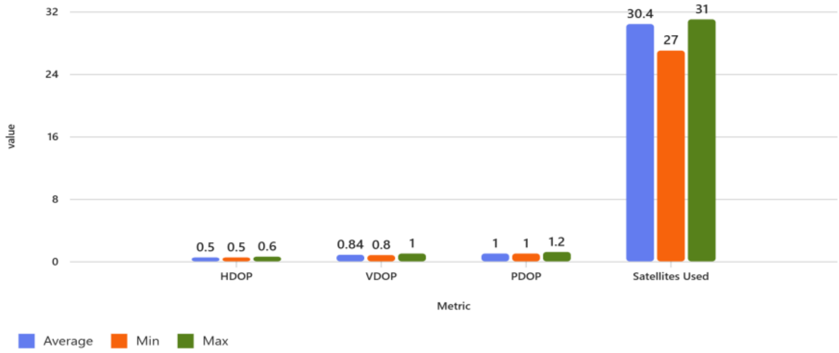

Şekil 13: *Birinci Test Dönüş Yönü GNSS Değerleri*

Birinci deney kapsamında, A–B referans hattına göre yanal geçiş hata dağılımları analiz edilmiştir. İleri ve geri geçişler sırasında elde edilen sapma değerlerinin zamansal değişimi, çizgi grafikleri kullanılarak sunulmuştur (Şekil 14 ve Şekil 15).

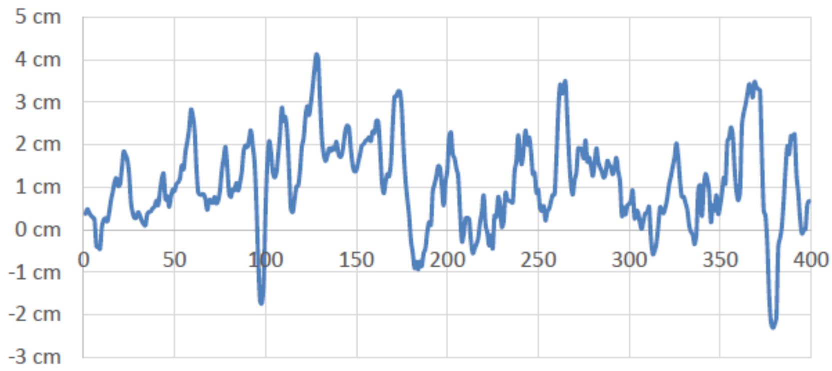

Şekil 14: *Gidiş Yönü – "A–B" Referans Hattından Sapma*

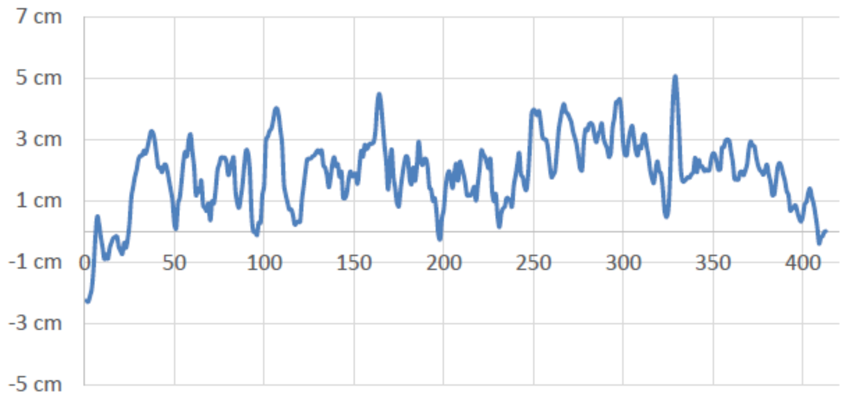

Şekil 15: *Dönüş Yönü – "A–B" Referans Hattından Sapma*

3.2. İlk Deneyden Bir Saat Sonra Gerçekleştirilen: İkinci Test Sonuçları

İkinci test kapsamında, ilk deneyden bir saat sonra otomatik dümenleme sisteminin (ODS) ileri ve geri geçişler sırasında elde edilen GNSS istatistikleri kaydedilmiştir. Elde edilen veriler, her bir geçiş için ayrı ayrı değerlendirilmiş ve grafiksel olarak sunulmuştur (Şekil 16 ve Şekil 17).

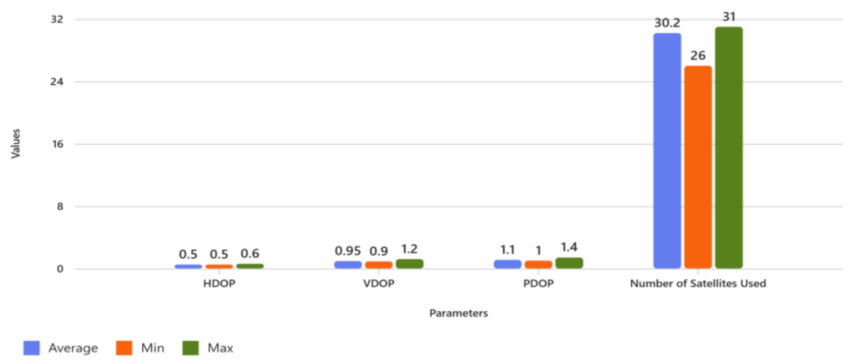

Şekil 16: *İkinci Test Gidiş Yönü GNSS Değerleri (1 Saat)*

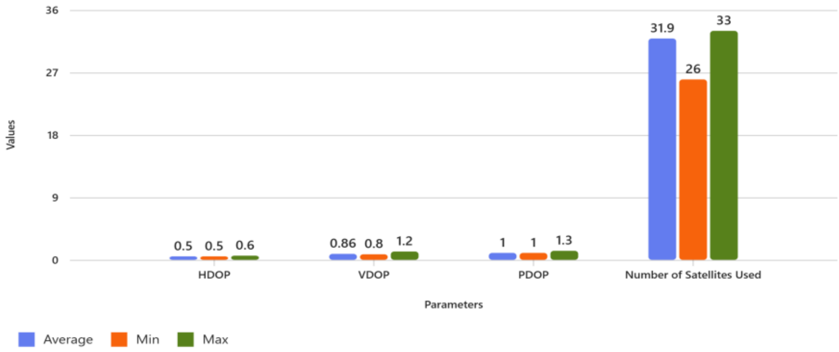

Şekil 17: *İkinci Test Dönüş Yönü GNSS Değerleri (1 Saat)*

İkinci deney kapsamında, ilk testten bir saat sonra A–B referans hattına göre yanal geçiş hata dağılımları analiz edilmiştir. İleri ve geri geçişler sırasında elde edilen sapma değerlerinin zamansal değişimi, çizgi grafikleri kullanılarak sunulmuştur (Şekil 18 ve Şekil 19).

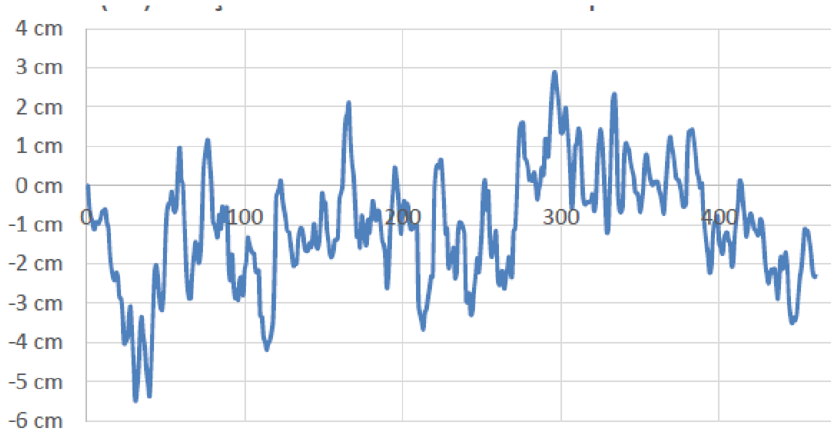

Şekil 18: *Gidiş Yönü – "A–B" Referans Hattından Sapma (1 Saat)*

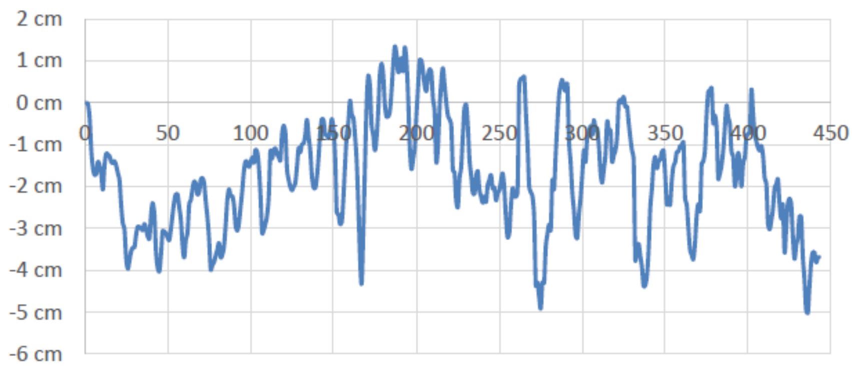

Şekil 19: *Dönüş Yönü – "A–B" Referans Hattından Sapma (1 Saat)*

3.3. İlk Deneyden 24 Saat Sonra Gerçekleştirilen: Üçüncü Test Sonuçları

Üçüncü test kapsamında, ilk deneyden yirmi dört saat sonra otomatik dümenleme sisteminin (ODS) ileri ve geri geçişler sırasında elde edilen GNSS istatistikleri kaydedilmiştir. Elde edilen veriler, her bir geçiş için ayrı ayrı değerlendirilmiş ve grafiksel olarak sunulmuştur (Şekil 20 ve Şekil 21).

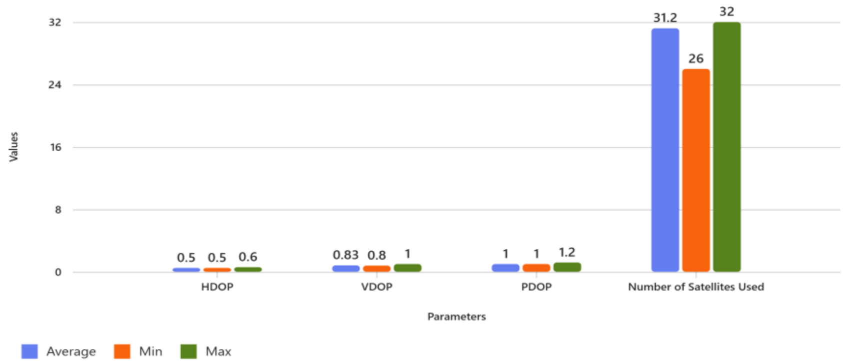

Şekil 20: *Üçüncü Test Gidiş Yönü GNSS Değerleri (24 Saat)*

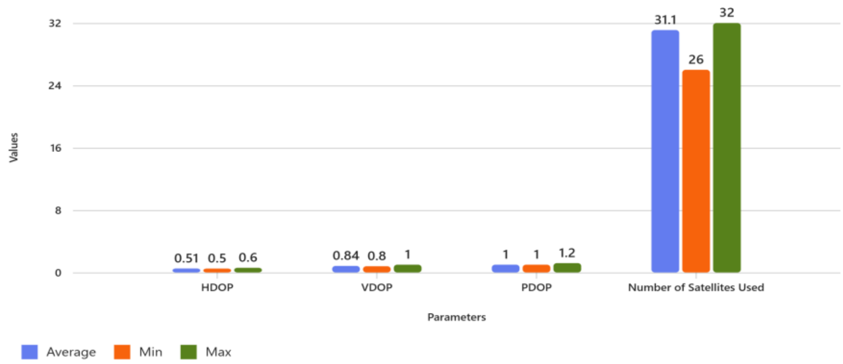

Şekil 21: *Üçüncü Test Dönüş Yönü GNSS Değerleri (24 Saat)*

Üçüncü deney kapsamında, ilk testten yirmi dört saat sonra A–B referans hattına göre yanal geçiş hata dağılımları analiz edilmiştir. İleri ve geri geçişler sırasında elde edilen sapma değerlerinin zamansal değişimi, çizgi grafikleri kullanılarak sunulmuştur (Şekil 22 ve Şekil 23).

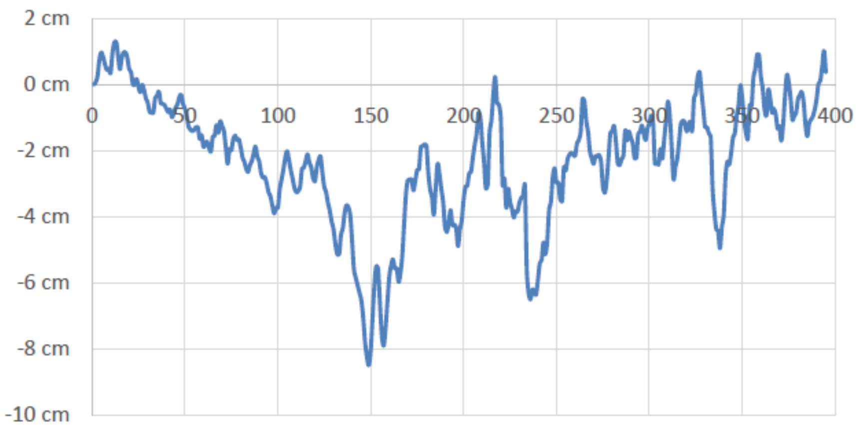

Şekil 22: *Gidiş Yönü – "A–B" Referans Hattından Sapma (24 Saat)*

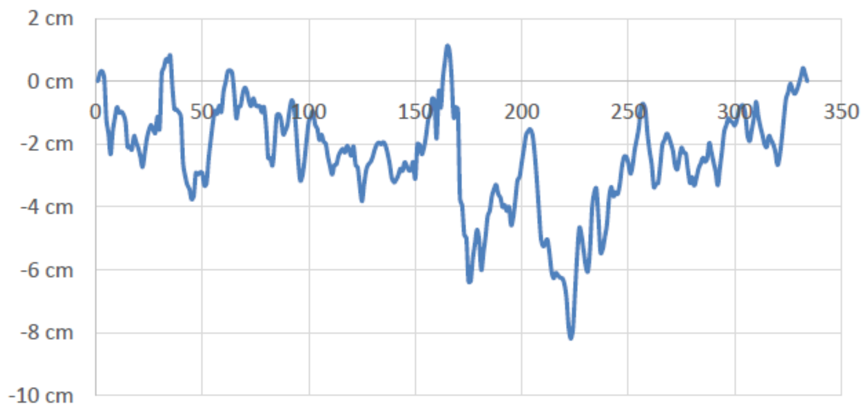

Şekil 23: *Dönüş Yönü – "A–B" Referans Hattından Sapma (24 Saat)*

4. Tartışma

Tarımda yönlendirme ve konumlandırma süreçleri, geleneksel olarak operatör deneyimine ve mekanik sistemlerin sınırlı hassasiyetine dayanmaktadır. Bu yaklaşım, uzun süreli operasyonlar sırasında doğrulukta azalmaya, tekrarlanabilirlik sorunlarına ve insan faktöründen kaynaklanan performans değişkenliğine yol açmaktadır. Dijitalleşmenin gelişmesiyle birlikte, bu sınırlamaları azaltmayı hedefleyen otomatik dümenleme sistemleri, tarımda önemli bir dönüşüm unsuru olarak ortaya çıkmıştır.

Otomatik dümenleme sistemlerinin gelişimi, yalnızca bir aracın önceden tanımlanmış bir güzergâh üzerinde tutulmasıyla sınırlı değildir. Bu tür sistemlerin, zamana bağlı kararlılık, geçişten geçişe tutarlılık ve değişken çevresel koşullar altında sürdürülebilir performans gibi kriterler açısından da değerlendirilmesi gerekmektedir. GNSS tabanlı konumlandırma teknolojilerindeki ilerlemeler sayesinde, tarımsal operasyonlardaki hassasiyet günümüzde hiç olmadığı kadar ölçülebilir ve karşılaştırılabilir hâle gelmiştir.

Bu bağlamda, elektrikli yönlendirme aktüasyon mekanizmaları ve sayısal kontrol mimarileri; geleneksel hidrolik ve manuel çözümlere kıyasla daha öngörülebilir ve tekrarlanabilir yönlendirme davranışı sunma potansiyeline sahiptir. Bu sistemlerin gelişimiyle birlikte etki alanı yalnızca operasyonel doğrulukla sınırlı kalmamakta; aynı zamanda operatör iş yükünün azaltılması, operasyonel sürekliliğin artırılması ve kullanıcı bağımlılığının minimize edilmesi gibi önemli kazanımları da beraberinde getirmektedir.

Bu nedenle, otomatik dümenleme sistemleri yalnızca mevcut tarımsal uygulamaların iyileştirilmesine yönelik araçlar olarak değil, aynı zamanda veri odaklı karar alma süreçleri ve geleceğin otonom tarım teknolojileri için temel bileşenler olarak değerlendirilmelidir. Bu çerçevede sunulan bulgular, sistemin mevcut durumunu yansıtmakla birlikte, ilerideki geliştirme potansiyelini ve tarımsal uygulamalar üzerindeki daha geniş etkisini de ortaya koymaktadır.

5. Sonuçlar

Yapılan testler, Otomatik Dümenleme Sisteminin, ISO 12188-2 standartlarına uygun olarak Erkunt Nimet 75Lux Deutz-V traktör modeli üzerinde başarıyla çalıştığını ortaya koymuştur. Sistem, GNSS (Küresel Navigasyon Uydu Sistemi) ve RTK (Gerçek Zamanlı Kinematik) düzeltme sinyallerinin entegrasyonu sayesinde hedeflenen ±2.5 cm konumlandırma hassasiyetini sağlamıştır.

Her bir test dizisi, aynı noktadan geçen RVP konum çiftlerinin zamansal olarak dengeli bir dağılımını sağlayacak şekilde kurgulanmış olup, bu yapı hata değerlerinin doğru bir biçimde hesaplanabilmesi açısından kritik öneme sahiptir. Testler kapsamında, A–B referans hattı boyunca gidiş ve dönüş yönünde 7.5 dakika olmak üzere belirlenen zaman sınırlarına uyulmuştur. Gidiş ve dönüş hareketleri sırasında kaydedilen RVP konumları arasındaki yatay mesafe farkı, test hattının göreceli enine iz hatası (Cross-Track Error – XTE) olarak tanımlanmıştır. Değerlendirmeye yalnızca, her iki yönde aynı noktadan geçişler arasındaki zaman farkı 15 dakikayı aşmayan veriler dâhil edilmiştir (Tablo 4) (Şekil 24 ve Şekil 25).

Tablo 4: *Deneylerin Genel Sonuçları*

Test	Ortalama Sapma (cm)	%50 Sapma (cm)	%95 Sapma (cm)	Maksimum Sapma (cm)	RMS Hatası (cm)	Standart Sapma (cm)	Veri Sayısı
I. Başlangıç	1.57	0.71	1.63	5.07	1.86	0.65	881
II. 1 Saat	1.66	1.29	1.89	5.48	2.01	1.14	948
III. 24 Saat	2.37	1.54	2.27	8.49	2.92	1.70	730
Ortalama	1.87	1.18	1.93	6.34	2.26	1.16	853
RMS	1.90	1.23	1.95	6.53	2.31	1.24	858
Standart Sapma	0.441	0.426	0.322	1.869	0.571	0.526	112

* Tüm test süresince seyir hızı 2,5 m/s olarak uygulanmıştır.

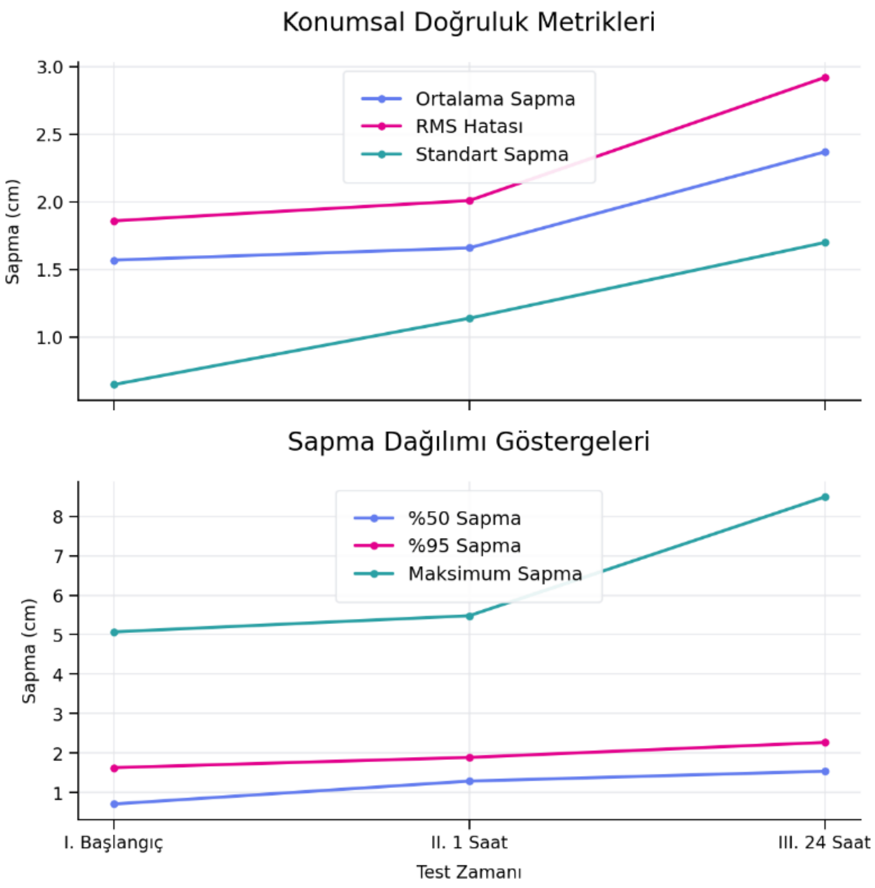

Şekil 24: *Konumsal Doğruluk Metrikleri*

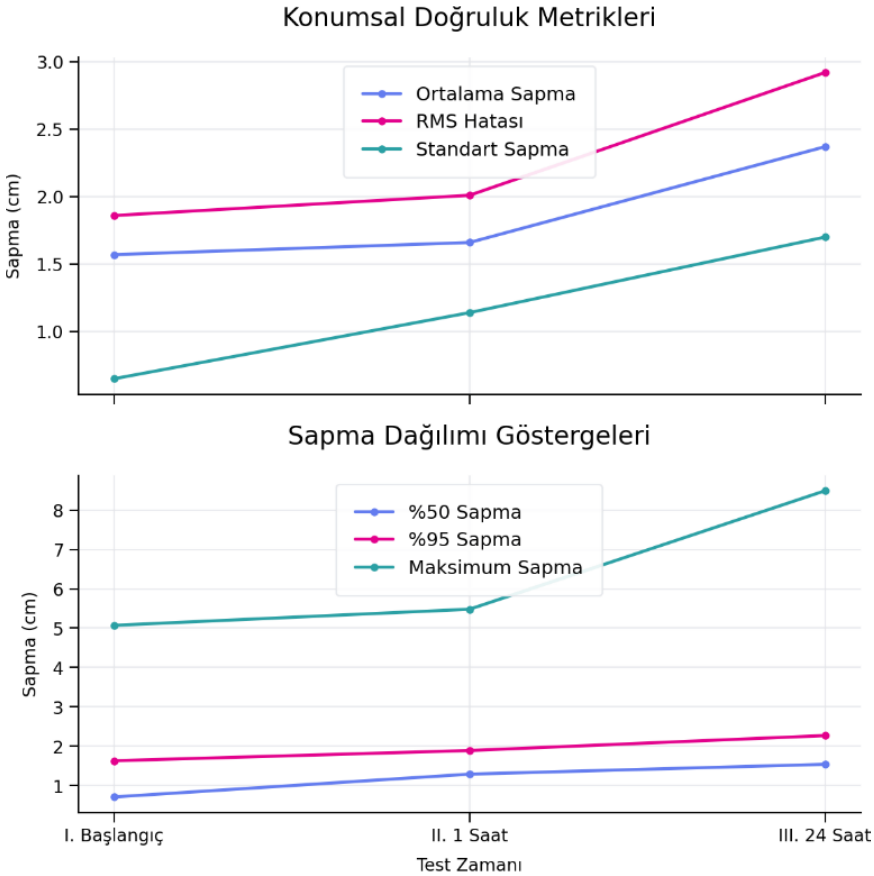

Şekil 25: *Sapma Dağılımı Göstergeleri*

Test edilen otomatik dümenleme sisteminin (ODS) performansını temsil eden %95 kümülatif sapma değeri 1,93 cm olarak belirlenmiştir.

STATEMENTS AND DECLARATIONS

Supplementary Material

No supplementary material accompanies this article.

Acknowledgements

Bu çalışmanın yürütülmesi sürecinde; saha testlerinin gerçekleştirilmesine, teknik altyapının sağlanmasına ve kurumsal imkânların kullanımına verdiği desteklerden dolayı Erkunt Traktör Sanayii A.Ş.'ye teşekkür ederim. Çalışma kapsamında elde edilen bulguların değerlendirilmesi ve akademik olarak sunulması süreci, tamamen yazarın sorumluluğunda olup, kurumun katkıları altyapı ve organizasyonel destek ile sınırlıdır.

Author Contributions

A. Mermer: Conceptualization, Methodology, Investigation, Field Testing, Formal Analysis, Writing – Original Draft, Writing – Review & Editing.

Conflicts of Interest

The author declares that there is no conflict of interest. The author is affiliated with Erkunt Traktör Sanayii A.Ş., whose equipment was used for field testing; the evaluation and academic presentation of the findings remain the sole responsibility of the author.

Data, Code & Protocol Availability

The data supporting the findings of this study are available from the corresponding author upon reasonable request.

Funding Received
This research did not receive any specific grant from funding agencies in the public, commercial, or not-for-profit sectors.

ORCID IDs
Ahmet Mermer https://orcid.org/0009-0002-5949-8926

REFERENCES
1. Y. Huang, J. Fu, S. Xu, T. Han, and Y. Liu, "Research on Integrated Navigation System of Agricultural Machinery Based on RTK-BDS/INS," Agriculture, vol. 12, no. 8, p. 1169, Aug. 2022, doi: 10.3390/agriculture12081169.
2. J. A. Thomasson, C. P. Baillie, D. L. Antille, C. R. Lobsey, and C. L. McCarthy, "Autonomous Technologies in Agricultural Equipment: A Review of the State of the Art," ASABE Distinguished Lecture Series, Tractor Design No. 40, American Society of Agricultural and Biological Engineers, 2019.
3. Z. Zhigang, H. Haixiang, L. Xiwen, et al., "Steering control system for a tractor using electric steering wheel," Transactions of the Chinese Society of Agricultural Engineering, vol. 40, no. 1, pp. 48–57, 2024, doi: 10.11975/j.issn.1002-6819.202309075.
4. S. Bhattacharya, R. G. Gallolukankanamalage, B. L. Steward, and M. Govindarasu, "ML-based Anomaly Detection for CAN Bus Network in Agriculture Machinery," Proceedings of the AAAI Symposium Series, vol. 4, no. 1, pp. 416–423, Nov. 2024, doi: 10.1609/aaaiss.v4i1.31826.
5. G. An, C. Yu, J. Du, X. Yin, Y. Ni, and C. Jin, "Development of the electric automatic steering system for agricultural vehicles," International Journal of Agricultural and Biological Engineering, vol. 17, no. 1, pp. 209–214, 2024, doi: 10.25165/j.ijabe.20241701.8493.
6. F. Radicioni, A. Stoppini, R. Brigante, A. Brozzi, and G. Tosi, "GNSS Network RTK for Automatic Guidance in Agriculture: Testing and Performance Evaluation," in Computational Science and Its Applications – ICCSA 2020, Lecture Notes in Computer Science, vol. 12253, Springer, pp. 19–35, Oct. 2020, doi: 10.1007/978-3-030-58814-4_2.

Aintelia Science Notes

ASNJ • BAUDER PRESS

Research Article

Comparative Investigation of Engine Compartment Insulation Materials on ECE R51 Pass-By Noise Performance of M3 Category Buses

Ecem Turhan Er[1,*], Samet Onur Emir[2]

1, 2 Güleryüz Karoseri Otomotiv San. ve Tic. A.Ş., Bursa, Türkiye

Correspondence to:
Ecem Turhan Er – ecem.turhan@guleryuz.com

How to Cite:
Actual Citation as taken from website

RECEIVED: 22/04/2026
ACCEPTED: 01/05/2026
PUBLISHED: 30/06/2026

ABSTRACT

Exterior vehicle noise regulations, particularly ECE R51, impose increasingly stringent limits on pass-by noise emissions, making acoustic insulation materials a critical design parameter in commercial vehicle development. In addition to acoustic performance, engine compartment insulation materials must also comply with fire safety requirements specified by ECE R107. This study presents a comparative investigation of two insulation materials commonly used in commercial vehicle engine compartments: closed-cell polyurethane foam and polyester nonwoven felt. A comprehensive review of commercially available insulation materials was initially conducted considering both acoustic performance and regulatory requirements. Based on this evaluation, two representative insulation solutions were selected for full-scale experimental validation. Two equivalent M3 category city buses equipped with identical 220 kW rear-mounted Mercedes diesel powertrains were tested under standardized ECE R51 pass-by noise conditions. Both insulation systems utilized a thickness of 30 mm and an aluminum-faced protective covering. The first configuration employed closed-cell polyurethane foam, while the second utilized polyester nonwoven felt. Noise measurements were performed according to ECE R51 requirements under homologation-level test conditions. A simplified acoustic prediction model based on frequency-dependent sound absorption coefficients was developed and validated through experimental testing. The results demonstrated that the polyester nonwoven insulation achieved a lower average pass-by noise level of 74.9 dB(A) compared to 79.5 dB(A) for the polyurethane foam configuration, corresponding to an overall improvement of approximately 4.6 dB. The improved performance was attributed to the superior sound absorption characteristics of the porous fibrous structure, particularly within the dominant engine noise frequency range of 1500–2000 Hz. The study provides practical guidance for acoustic insulation material selection in commercial vehicle applications and demonstrates the importance of considering both acoustic performance and regulatory compliance during engine compartment insulation design.

KEYWORDS

ECE R51, ECE R107, Pass-by Noise, Acoustic Insulation, Polyester Nonwoven Felt, Polyurethane Foam, M3 Bus

1. Introduction

Vehicle exterior noise has become an increasingly important environmental issue due to its impact on urban acoustic comfort, public health, and environmental sustainability. Road traffic noise generated by heavy commercial vehicles is one of the major contributors to environmental noise pollution, particularly in densely populated urban areas. Consequently, international regulations such as UN/ECE Regulation No. 51 impose progressively stricter limits on vehicle pass-by noise emissions in order to reduce the environmental impact of road transportation systems [1–3].

For heavy-duty M3 category buses, compliance with ECE R51 Phase 3 requirements represents a significant engineering challenge. During pass-by noise testing, vehicle exterior noise is influenced by several factors including engine power output, combustion characteristics, cooling system operation, exhaust noise, and engine compartment acoustic insulation performance [4,5]. In rear-engine diesel buses, the engine compartment is one of the dominant noise sources contributing to measured pass-by noise levels, particularly within the frequency range associated with combustion and mechanical excitation.

In addition to acoustic performance requirements, insulation materials installed within the engine compartment must satisfy fire safety requirements. According to ECE R107, flammable sound-proofing materials or materials liable to become impregnated with fuel, lubricant, or other combustible substances shall not be used in the engine compartment unless adequately protected by an impermeable covering [6]. Consequently, material selection for engine compartment applications requires a balance between acoustic absorption performance, durability, and regulatory compliance.

Various acoustic insulation materials are currently used in commercial vehicle engine compartments, including polyurethane foams, polyester nonwoven felts, melamine foams, glass fiber mats, mineral wool-based insulation systems, and recycled PET acoustic felts. These materials exhibit different sound absorption characteristics depending on their internal morphology, airflow resistivity, density, and frequency-dependent behavior [7–11].

Table 1: *Comparison of common engine compartment acoustic insulation materials used in commercial vehicles*

Material	Structure	Typical Sound Absorption Coefficient @1000 Hz	Effective Frequency Range (Hz)	Fire Performance	ECE R107 Suitability
Closed-cell Polyurethane Foam	Closed-cell	0.20–0.35	1000–4000	Moderate	Requires protective covering
Open-cell Polyurethane Foam	Open-cell	0.60–0.90	500–4000	Moderate	Requires protective covering
Polyester Nonwoven Felt	Open fibrous	0.75–0.95	500–3000	Good	Suitable when protected
Melamine Foam	Open-cell	0.80–1.00	500–5000	Excellent	Suitable
Glass Fiber Mat	Fibrous	0.85–1.00	250–4000	Excellent	Suitable
Mineral Wool	Fibrous	0.85–1.00	250–4000	Excellent	Suitable
Recycled PET Acoustic Felt	Open fibrous	0.70–0.95	500–3000	Good	Suitable when protected

Among these materials, polyester nonwoven structures and melamine foams generally exhibit superior acoustic absorption performance due to their open porous morphology, while closed-cell polyurethane foams provide comparatively lower acoustic absorption but offer advantages in thermal insulation and mechanical durability [8–12].

However, despite the availability of acoustic characterization data under laboratory conditions, limited studies have investigated the influence of these materials on full-scale vehicle pass-by noise performance under homologation-level ECE R51 testing conditions.

Therefore, this study focuses on two insulation solutions widely used in commercial vehicle applications and capable of meeting engine compartment installation requirements: closed-cell polyurethane foam and polyester nonwoven felt. The objective is to investigate the relationship between material acoustic properties and measured vehicle exterior noise emissions and to provide practical guidance for insulation material selection in future commercial vehicle developments targeting compliance with ECE R51 Phase 3 requirements.

2. Materials and Methods

Test Vehicle Specifications

The experimental study was conducted using two equivalent M3 category city buses developed on the same vehicle platform.

Table 2: *Vehicle Specifications*

Parameter	Value
Vehicle Category	M3 City Bus
Engine Type	Mercedes Diesel
Maximum Engine Power	220 kW
Engine Speed at Maximum Power	1800 rpm
Transmission	Automatic
Engine Compartment Volume	4 m³
Insulation Area	8 m²

According to ECE R51 requirements, pass-by noise measurements were performed while the engine operated within 85–89% of the engine speed at maximum power, corresponding to approximately 1530–1600 rpm during acceleration tests. Simultaneously, vehicle speed at the BB' line was maintained within 35 ± 5 km/h.

Under these operating conditions, dominant combustion, mechanical, cooling fan, and powertrain-related noise components were concentrated primarily within the 1500–2000 Hz frequency range.

Insulation Configurations

Two insulation configurations were comparatively evaluated.

Table 3: *Insulation Configurations*

Configuration	Insulation Material	Structure	Thickness
A	Polyurethane Foam	Closed-cell	30 mm
B	Polyester Nonwoven Felt	Open fibrous	30 mm

Both insulation systems employed identical aluminum-faced protective coverings in order to satisfy engine compartment durability and contamination protection requirements. Therefore, the observed acoustic performance differences can primarily be attributed to the acoustic behavior of the underlying insulation materials.

Acoustic Material Properties

The frequency-dependent sound absorption coefficients of both materials were evaluated according to representative literature and manufacturer data.

Table 4: *Frequency-Dependent Sound Absorption Coefficients*

Frequency (Hz)	Polyurethane Foam	Polyester Nonwoven Felt
500	0.15	0.57
1000	0.25	0.84
1200	0.30	0.82
1500	0.35	0.93
2000	0.40	0.84

The polyester nonwoven felt exhibits significantly higher absorption performance within the frequency range associated with dominant diesel engine noise.

ECE R51 Pass-By Noise Test Procedure

Exterior vehicle noise measurements were conducted in accordance with UN/ECE Regulation No. 51 Revision 3 under ISO 10844 compliant test track conditions. Microphones were positioned 7.5 m from the vehicle centerline and 1.2 m above ground level. Measurements were obtained separately from both sides of the vehicle and repeated four times for each configuration. Environmental conditions satisfied all ECE R51 requirements regarding wind speed, ambient temperature, and background noise levels.

Prior to the pass-by noise evaluation, reference engine noise measurements were conducted under stationary operating conditions. The engine was operated at 1800 rpm, corresponding to the engine speed at maximum power, while the engine compartment cover was kept open. The microphone position was maintained consistent with the ECE R51 measurement geometry. Under these conditions, the measured reference engine noise level was approximately 81.0 dB(A), while the direct engine noise level was measured as 81.5 dB(A). These measurements were subsequently used as reference inputs for the acoustic prediction model.

Acoustic Evaluation Approach

The acoustic performance of the investigated insulation materials was evaluated using a simplified absorption-based prediction model combined with experimental ECE R51 pass-by noise measurements. The sound absorption coefficient is defined as [8]:

$$\alpha = 1 - Ir / Ii \qquad (1)$$

where Ii represents the incident sound intensity and Ir represents the reflected sound intensity. The equivalent acoustic absorption area is expressed as [13]:

$$A = \alpha S \qquad (2)$$

where A is the equivalent absorption area, α is the sound absorption coefficient, and S is the insulation surface area. Noise reduction was evaluated using [14]:

$$NR = L1 - L2 \qquad (3)$$

where L1 and L2 represent sound pressure levels before and after insulation application. A simplified absorption-based prediction model was employed using the measured reference engine noise level of 81.0 dB(A) as the baseline condition. The dominant operating frequency observed during the ECE R51 tests was approximately 2000 Hz. Therefore, the absorption coefficients at 2000 Hz were used for the theoretical comparison. The predicted sound pressure levels were calculated according to:

$$L2 = L1 + 10 \log10((1 - \alpha2) / (1 - \alpha1)) \qquad (4)$$

where L1 = reference sound pressure level, L2 = predicted sound pressure level after insulation, α1 = absorption coefficient of the reference condition, α2 = absorption coefficient of the investigated insulation material. For the reference condition without insulation:

$$\alpha 1 = 0 \quad (5)$$

The measured reference engine noise level was L1 = 81.0 dB(A). Using the sound absorption coefficients at 2000 Hz from Table 4, the predicted sound pressure levels were calculated as follows.

Polyurethane Foam:

$$L\_PU = 81 + 10 \log 10((1 - 0.40) / (1 - 0)) \quad (6)$$

$$L\_PU = 81 + 10 \log 10(0.60) \quad (7)$$

$$L\_PU = 78.8 \ dB(A) \quad (8)$$

Polyester Nonwoven Felt:

$$L\_PET = 81 + 10 \log 10((1 - 0.84) / (1 - 0)) \quad (9)$$

$$L\_PET = 81 + 10 \log 10(0.16) \quad (10)$$

$$L\_PET = 73.0 \ dB(A) \quad (11)$$

Table 5: *Predicted acoustic performance based on absorption coefficients*

Configuration	Absorption Coefficient at 2000 Hz	Predicted SPL (dB(A))
Reference (No Insulation)	0.00	81.0
Polyurethane Foam	0.40	78.8
Polyester Nonwoven Felt	0.84	73.0

The calculated results indicate that polyester nonwoven felt is expected to provide significantly greater acoustic attenuation due to its higher absorption coefficient at the dominant operating frequency. These predicted values were subsequently validated through full-scale ECE R51 pass-by noise measurements presented in the following section.

Figure 1: *ECE R51 pass-by noise test setup showing the microphone position at the test track during vehicle noise measurements.*

3. Results

Pass-by noise measurements were performed under identical ECE R51 test conditions for both insulation configurations. During all measurements, the vehicle was operated in third gear with a vehicle speed of approximately 24 km/h at the AA' line and 32 km/h at the BB' line. The engine speed at the BB' line was maintained at approximately 1550 rpm for all test runs, ensuring consistent operating conditions throughout the experiments.

The results obtained for the polyurethane foam insulation configuration are presented below. Four consecutive measurements were conducted from both the left and right sides of the vehicle. The average sound pressure levels were determined as 76.3 dB(A) on the right side and 82.7 dB(A) on the left side, resulting in an overall average pass-by noise level of 79.5 dB(A).

Table 6: *Experimental ECE R51 Pass-By Noise Results — Polyurethane Foam + Aluminum Facing Insulation*

Run	Lmax right side (dB(A))	Lmax left side (dB(A))	Vaa' (km/h)	Vbb' (km/h)	Nbb' (min^{-1})
1	76.3	82.6	24	32	1550
2	76.2	83.0	24	32	1550
3	76.2	82.7	24	32	1550
4	76.3	82.6	24	32	1550
Average	76.3	82.7			
Total Average	79.5				

Table 7: *Experimental ECE R51 Pass-By Noise Results — Polyester Nonwoven Felt + Aluminum Facing Insulation*

Run	Lmax right side (dB(A))	Lmax left side (dB(A))	Vaa' (km/h)	Vbb' (km/h)	Nbb' (min^{-1})
1	73.7	76.5	24	32	1550
2	73.5	75.7	24	32	1550
3	73.9	76.0	24	32	1550
4	73.8	75.8	24	32	1550
Average	73.7	76.0			
Total Average	74.9				

The results obtained for the polyester nonwoven felt insulation configuration show that the average sound pressure levels were measured as 73.7 dB(A) on the right side and 76.0 dB(A) on the left side, resulting in an overall average pass-by noise level of 74.9 dB(A).

A comparison of the two insulation systems indicates that the polyester nonwoven felt configuration achieved the lowest overall exterior noise level. Relative to the polyurethane foam configuration, the measured pass-by noise level decreased from 79.5 dB(A) to 74.9 dB(A).

Table 8: *Predicted and Measured Pass-By Noise Levels*

Configuration	Predicted SPL (dB(A))	Measured SPL (dB(A))	Deviation (dB)
Polyurethane Foam	78.8	79.5	0.7
Polyester Nonwoven Felt	73.0	74.9	1.9

The simplified absorption-based prediction model showed good agreement with the experimental measurements. The maximum deviation between predicted and measured pass-by noise levels remained below 2 dB, indicating that frequency-dependent sound absorption coefficients can provide a useful first-order indicator for evaluating engine compartment acoustic insulation performance.

An additional observation was the difference between the left and right side measurements. The polyurethane foam configuration exhibited a side-to-side difference of approximately 6.4 dB, whereas the polyester nonwoven felt configuration reduced this difference to approximately 2.3

dB. This behavior suggests a more homogeneous acoustic energy dissipation mechanism within the engine compartment when porous fibrous insulation materials are utilized.

4. Discussion and Conclusion

The results clearly demonstrate that insulation material selection significantly affects exterior vehicle noise performance under ECE R51 pass-by testing conditions.

Although both configurations employed identical aluminum-faced protective coverings, the polyester nonwoven insulation provided substantially improved acoustic performance compared with the closed-cell polyurethane foam. This improvement is attributed to the porous fibrous morphology of polyester nonwoven materials, which enables enhanced viscous and thermal dissipation of acoustic energy.

The higher sound absorption coefficients observed within the 1500–2000 Hz frequency range correspond closely with the dominant noise frequencies generated by diesel engine combustion, mechanical operation, and cooling systems during ECE R51 acceleration tests. Consequently, the superior absorption behavior of polyester nonwoven felt translated directly into reduced exterior noise emissions.

From a regulatory perspective, the investigated materials must satisfy both acoustic performance requirements specified by ECE R51 and engine compartment safety requirements specified by ECE R107. The use of aluminum-faced coverings provides protection against contamination by fuel, lubricant, and other combustible substances while maintaining acoustic functionality.

Relative to the reference engine noise level of 81.0 dB(A), the polyurethane foam configuration achieved a reduction of approximately 1.5 dB, whereas the polyester nonwoven felt configuration achieved a reduction of approximately 6.1 dB. The measured improvement is consistent with the significantly higher absorption coefficient of polyester felt at the dominant operating frequency of approximately 2000 Hz.

The measured reduction of approximately 4.6 dB between the two insulation configurations represents a significant improvement in pass-by noise performance and may contribute substantially toward compliance with future ECE R51 Phase 3 limits.

In conclusion, polyester nonwoven felt demonstrated superior acoustic performance compared with closed-cell polyurethane foam under homologation-level ECE R51 testing conditions. The measured pass-by noise level was reduced from 79.5 dB(A) to 74.9 dB(A), corresponding to an improvement of approximately 4.6 dB. Furthermore, the simplified prediction model showed good agreement with experimental measurements, with deviations remaining below 2 dB. The findings highlight the importance of porous acoustic material selection in commercial vehicle development and provide practical guidance for future engine compartment insulation optimization targeting compliance with both ECE R51 and ECE R107 requirements.

STATEMENTS AND DECLARATIONS

Supplementary Material

No supplementary material accompanies this article.

Acknowledgements

The authors would like to thank Güleryüz Karoseri Otomotiv A.Ş. for providing the test vehicles, engineering support, and homologation testing resources used throughout this study.

Author Contributions

E. Turhan Er: Conceptualization, Methodology, Investigation, Formal Analysis, Writing – Original Draft, Writing – Review & Editing. S. O. Emir: Methodology, Investigation, Homologation Testing, Writing – Review & Editing.

Conflicts of Interest

The authors declare that there is no conflict of interest. The authors are affiliated with Güleryüz Karoseri Otomotiv Sanayi ve Ticaret A.Ş., whose vehicles and test facilities were used in this study.

Data, Code & Protocol Availability

The data supporting the findings of this study are available from the corresponding author upon reasonable request.

Funding Received

This research did not receive any specific grant from funding agencies in the public, commercial, or not-for-profit sectors.

ORCID IDs

Ecem Turhan Er https://orcid.org/0009-0002-8113-5697
Samet Onur Emir https://orcid.org/0009-0005-5316-1670

REFERENCES

1. M. S. Qatu, "Overview of automotive noise and vibration," Int. J. Veh. Noise Vib., vol. 5, no. 1, pp. 1–35, 2009, doi: 10.1504/IJVNV.2009.029187.
2. M. E. Braun, S. J. Walsh, J. L. Horner, and R. Chuter, "Noise source characteristics in the ISO 362 vehicle pass-by noise test: Literature review," Appl. Acoust., vol. 74, no. 11, pp. 1241–1265, 2013, doi: 10.1016/j.apacoust.2013.04.005.
3. United Nations Economic Commission for Europe (UNECE), UN Regulation No. 51: Uniform Provisions Concerning the Approval of Motor Vehicles Having at Least Four Wheels with Regard to Their Sound Emissions, Revision 3, Geneva, Switzerland: UNECE, 2024.
4. International Organization for Standardization, ISO 362-1:2015 — Measurement of Noise Emitted by Accelerating Road Vehicles — Engineering Method — Part 1: M and N Categories, Geneva, Switzerland: ISO, 2015.
5. J. Pang, Noise and Vibration Control in Automotive Bodies. Hoboken, NJ, USA: Wiley, 2014.
6. United Nations Economic Commission for Europe (UNECE), UN Regulation No. 107: Uniform Provisions Concerning the Approval of Category M2 and M3 Vehicles with Regard to Their General Construction, Geneva, Switzerland: UNECE, 2024.
7. J. P. Arenas and M. J. Crocker, "Recent trends in porous sound-absorbing materials," Sound Vib., vol. 44, no. 7, pp. 12–18, 2010.
8. J. F. Allard and N. Atalla, Propagation of Sound in Porous Media: Modelling Sound Absorbing Materials, 2nd ed. Chichester, U.K.: Wiley, 2009.
9. U. Berardi and G. Iannace, "Acoustic characterization of natural fibers for sound absorption applications," Build. Environ., vol. 94, pp. 840–852, 2015, doi: 10.1016/j.buildenv.2015.05.029.
10. M. Tascan and E. A. Vaughn, "Effects of total surface area and fabric density on the acoustical behavior of needle-punched nonwoven fabrics," Text. Res. J., vol. 78, no. 4, pp. 289–296, 2008, doi: 10.1177/0040517507084283.
11. L. Cao, Q. Fu, Y. Si, B. Ding, and J. Yu, "Porous materials for sound absorption," Compos. Commun., vol. 10, pp. 25–35, 2018, doi: 10.1016/j.coco.2018.05.001.
12. L. J. Gibson and M. F. Ashby, Cellular Solids: Structure and Properties, 2nd ed. Cambridge, U.K.: Cambridge Univ. Press, 1997.
13. T. J. Cox and P. D'Antonio, Acoustic Absorbers and Diffusers: Theory, Design and Application, 3rd ed. Boca Raton, FL, USA: CRC Press, 2016.
14. L. L. Beranek and I. L. Vér, Eds., Noise and Vibration Control Engineering: Principles and Applications, 2nd ed. Hoboken, NJ, USA: Wiley, 2006.

Aintelia Science Notes

ASNJ • BAUDER PRESS

Research Article

Ticari Panelvan Araçlar İçin Havalandırma Performansının CAE Tabanlı Analizi ve Tasarım Optimizasyonu

CAE-Based Analysis and Design Optimization of Ventilation Performance for Commercial Panel Vans

Ümmet Ayyıldız[1], Songül Kılınç[2,*], Kadir Güyen[3]

1,2,3 OTM Plastik Tasarım Merkezi

Correspondence to:
Songül Kılınç – songul.kilinc@otmplastik.com.tr

How to Cite:
Actual Citation as taken from website

RECEIVED: 24/04/2026
ACCEPTED: 01/05/2026
PUBLISHED: 30/06/2026

ABSTRACT

In the commercial vehicle segment, particularly in panel vans used for school and personnel transportation, the interior volume of approximately 15 m³ makes the design of interior trim components critical in terms of in-cabin comfort, interior climate control, and airflow rate. In this context, with the introduction of a new design, the development of lightweight and functional interior trim components has emerged as an important engineering challenge in order to both reduce vehicle weight and improve climate control performance. In this study, the design optimization of ventilation components integrated into the interior trim system of 15 m³ panel vans and minibus are investigated. During the analysis process, computer-aided engineering (CAE) methods were employed, and the effects of different design parameters on airflow performance were numerically examined. In order to improve in-cabin air circulation, ventilation duct diameters and vent geometries were evaluated. Accordingly, duct diameters were defined as 50 mm and 70 mm, while vent geometries were modeled as circular and rectangular cross-sections. The results of the flow analyses indicated that the design with a 70 mm duct diameter and a circular vent with a diameter of 68 mm provided the best performance in terms of airflow distribution, pressure loss, and flow uniformity. The findings demonstrate the direct impact of geometric parameters in interior trim design on air quality and passenger comfort. The optimized design approach offers significant contributions in terms of more efficient ventilation, improved passenger comfort, and potential energy savings in service vehicles. It is expected that this study will guide future optimization efforts and interior trim design processes in commercial vehicles.

KEYWORDS

Flow optimization, Cabin comfort, CAE (Computer-Aided Engineering), Airflow analysis, Interior trim design

ÖZET

Ticari araç segmentinde yer alan ve özellikle okul ile personel servis taşımacılığında kullanılan panelvan tipi araçlarda, iç hacmin yaklaşık 15 m^3 seviyesinde olması, araç içi konfor iç ortam iklimlendirme hava debisi açısından iç trim komponentlerinin tasarımını kritik hale getirmektedir. Bu kapsamda yeni dizayn ile beraber, hem araç ağırlığının azaltılması hem de iklimlendirme performansın artırılması amacıyla hafifletilmiş ve fonksiyonel iç trim parçalarının geliştirilmesi önemli bir mühendislik problemi olarak öne çıkmaktadır. Bu çalışmada, 15 m^3 panelvan ve minibüs araçlar için iç trim sistemine entegre edilen havalandırma bileşenlerinin tasarım optimizasyonu ele alınmıştır. Analiz sürecinde bilgisayar destekli mühendislik (CAE) yöntemleri kullanılmış ve farklı tasarım parametrelerinin hava akış performansına etkisi sayısal olarak incelenmiştir. Araç içi hava sirkülasyonunun iyileştirilmesi amacıyla, havalandırma boru çapları ve menfez geometrileri değerlendirilmiştir. Bu doğrultuda, boru çapı parametresi 50 mm ve 70 mm olarak belirlenmiş; menfez geometrileri ise dairesel ve dikdörtgen kesitli olacak şekilde modellenmiştir. Gerçekleştirilen akış analizleri sonucunda, 70 mm boru çapı ve 68 mm çapında dairesel menfez kullanılan tasarımın, hava akış dağılımı, basınç kaybı ve homojenlik açısından en iyi performansı sağladığı tespit edilmiştir. Elde edilen bulgular, iç trim tasarımında geometrik parametrelerin hava kalitesi ve yolcu konforu üzerindeki doğrudan etkisini ortaya koymaktadır. Optimize edilen bu tasarım yaklaşımı, servis araçlarında daha verimli havalandırma, artırılmış yolcu konforu ve potansiyel enerji tasarrufu sağlama açısından önemli katkılar sunmaktadır. Çalışmanın, ticari araç iç trim tasarım süreçlerine ve gelecekte yapılacak optimizasyon çalışmalarına rehberlik etmesi beklenmektedir.

Anahtar Kelimeler: Akış Optimizasyonu, Araç İçi Konfor, CAE (Bilgisayar Destekli Mühendislik), Hava akışı analizi, İç trim tasarımı

1. GİRİŞ

Ticari araç sektöründe, özellikle okul ve personel taşımacılığında kullanılan panelvan tipi araçlarda yolcu konforu ve iç ortam hava kalitesi, tasarım süreçlerinin temel belirleyicilerinden biri haline gelmiştir. Araç iç hacminin yaklaşık 15 m³ seviyesinde olması, iklimlendirme sistemlerinin etkinliğini doğrudan etkileyerek homojen hava dağılımı ve yeterli hava sirkülasyonunun sağlanmasını zorlaştırmaktadır. Araç kabinlerinin yeterli havalandırılmaması durumunda karbondioksit (CO_2) konsantrasyonunun hızla artabildiği ve bunun sürücü dikkatinde azalma ve reaksiyon süresinde gecikme gibi güvenlik risklerine yol açabileceği açıkça ortaya konmuştur [1]. Araç içerisinde kullanılan koltuk sayısı göz önüne alındığında, bu durum, yalnızca termal konfor açısından değil, aynı zamanda yolcu sağlığı ve güvenliği açısından da kritik bir mühendislik problemi olarak değerlendirilmektedir [2,3]. Yetersiz havalandırma durumunda CO_2 konsantrasyonunun hızla artarak sürücü dikkatini ve yolcu konforunu olumsuz etkilediği gösterilmiştir [4].

Literatürde, araç içi hava kalitesinin ve termal konforun; hava akış dağılımı, hız profilleri ve sıcaklık homojenliği gibi parametrelerle doğrudan ilişkili olduğu gibi araç içi malzemelerden kaynaklanan emisyonlar ve dış ortamdan gelen kirleticiler de kabin hava kalitesini doğrudan etkilemektedir [5]. Özellikle kapalı alanlarda yetersiz hava sirkülasyonu, CO_2 birikimi ve kirletici yoğunluğunun artmasına neden olmakta, bu durum da yolcu konforunu ve bilişsel performansı olumsuz etkileyebilmektedir [6]. Bu bağlamda, havalandırma sistemlerinin tasarımında menfez yerleşimi, kanal geometrisi ve kesit özellikleri kritik rol oynamaktadır.

Son yıllarda, bilgisayar destekli mühendislik (CAE) ve özellikle Hesaplamalı Akışkanlar Dinamiği (CFD) yöntemleri, otomotiv iç ortam hava akışının analizinde yaygın olarak kullanılmaktadır. Bir CFD çalışmasında, özellikle resirkülasyon modunda çalışılan sistemlerde CO_2 seviyesinin hızlı şekilde yükseldiği, buna karşılık taze hava modunun ise dış ortamdan partikül girişini artırdığı gösterilmiştir [7]. Diğer bir çalışmada, menfez sayısı, konumu ve geometrisinin hava dağılımını doğrudan etkilediği ve bu parametrelerin tasarım sürecinde kritik rol oynadığı da deneysel ve sayısal çalışmalarla ortaya konmuştur [8]. Araç HVAC sistemlerinin tasarımında kanal geometrisi, menfez yerleşimi ve hava debisinin hem yolcu konforu hem de enerji tüketimi üzerinde belirleyici olduğu vurgulanmaktadır. CFD tabanlı analizlerin kullanıldığı çalışmalar, havalandırma sistemlerinin optimize edilmesiyle kabin içerisindeki hava değişim oranının artırılabildiğini ve böylece daha güvenli ve konforlu bir iç ortam sağlanabildiğini göstermektedir [9].

Bu doğrultuda, panelvan tipi ticari araçlarda iç trim sistemine entegre edilen havalandırma bileşenlerinin tasarımı, yalnızca mekanik bir gereklilik değil, aynı zamanda çok parametreli bir optimizasyon problemi olarak ele alınmaktadır. Bu çalışmada, farklı geometrik tasarım parametrelerinin hava akış performansı üzerindeki etkileri literatür bulguları ışığında incelenerek, optimum tasarım yaklaşımının belirlenmesi amaçlanmıştır.

2. MATERYAL VE YÖNTEM

Bilgisayar destekli analiz yöntemi, nümerik bir çözümleme metodu olup ideal durumlar dahilinde işlem yapmaktadır. Bu sebeple sistemlerin kıyaslanması açısından önemli bir yere sahiptir.

Şekil 1: Klima menfez sistemi

Klima menfez sistemi üzerinden (Şekil 1) sağ ve sol menfez hatlarından çıkan açıklıklardan çıkan hava hızları 3 farklı model için analiz edilecektir. Tablo 1'de belirlenen modeller için analizler gerçekleştirilmiştir.

Tablo 1: Analiz edilecek menfez sistemi modelleri

Model 1	Model 2	Model 3
Boru Çapı: 50 mm	Boru Çapı: 70 mm	Boru Çapı: 70 mm
Menfez: Dikdörtgen	Menfez: Dikdörtgen	Menfez: Daire (68 mm)
Klima İç Ayrım (Hava ayırma perdesi): Yok	Klima İç Ayrım (Hava ayırma perdesi): Var	Klima İç Ayrım (Hava ayırma perdesi): Var

Sayısal analizlerin doğruluğunu ve güvenilirliğini sağlamak amacıyla, çalışma kapsamında oluşturulan üç boyutlu model üzerinde detaylı bir ağ (mesh) yapısı oluşturulmuştur. Ağ oluşturma sürecinde, çözüm hassasiyeti ile hesaplama maliyeti arasında optimum dengeyi sağlamak hedeflenmiştir. Bu doğrultuda, model geometrisinin karmaşıklığı, akış bölgelerindeki hız gradyentleri ve sınır tabaka etkileri dikkate alınarak hibrit bir ağ yapısı tercih edilmiştir.

Ağ modeli toplam 1.218.433 elemandan oluşmakta olup, çözüm doğruluğunu artırmak amacıyla kritik bölgelerde yerel ağ inceltme (local refinement) uygulanmıştır. Özellikle havalandırma kanalları, menfez çıkışları ve akışın yön değiştirdiği bölgelerde daha küçük eleman boyutları kullanılarak akış karakteristiğinin daha hassas yakalanması sağlanmıştır. Bu kapsamda, ağ yapısında maksimum eleman boyutu 10 mm, minimum eleman boyutu ise 0,1 mm olarak tanımlanmıştır.

Minimum eleman boyutunun, özellikle sınır tabaka bölgelerinde ve yüksek hız gradyentinin bulunduğu alanlarda kullanılmasıyla, viskoz etkilerin ve türbülans yapısının daha doğru modellenmesi amaçlanmıştır. Buna karşılık, akışın daha homojen olduğu hacimsel bölgelerde daha büyük elemanlar kullanılarak toplam çözüm süresi optimize edilmiştir.

Tablo 2: Ağ modelinin oluşturulması

Parametre	Değer
Toplam Eleman	1.218.433
Maksimum Eleman Boyutu	10 mm
Minimum Eleman Boyutu	0,1 mm

Sınır şartları olarak, akışkan ortam olarak hava tanımlanmış olup, sistemde hava hareketi blower fan aracılığıyla sağlanmıştır. Blower fan devri 3000 rpm olarak belirlenmiş ve bu değer analizlerde sabit sınır şartı olarak uygulanmıştır. Çalışma, araç kabini içerisindeki hava akış karakteristiğini incelemek amacıyla dış akış (external flow) analizi kapsamında ele alınmıştır. Analizlerde zamana bağlı değişimlerin incelenebilmesi için çözüm yöntemi geçici rejim olarak seçilmiştir. Türbülans etkilerinin modellenmesinde ise mühendislik uygulamalarında yaygın olarak tercih edilen k-ε (k-epsilon) türbülans modeli kullanılmıştır [10]. Zamana bağlı çözüm sürecinde toplam analiz süresi 5 saniye olarak tanımlanmış olup, çözüm hassasiyetini artırmak amacıyla zaman adımı 0,01 saniye olarak belirlenmiştir. Her bir zaman adımı için 10 iterasyon gerçekleştirilmiş ve bu doğrultuda toplam iterasyon sayısı 5000 olarak hesaplanmıştır. Belirlenen bu sınır şartları ve çözüm parametreleri ile, sistemdeki hava akışının zamana bağlı davranışı, hız dağılımı ve akış homojenliği güvenilir bir şekilde analiz edilmiştir.

3. SONUÇLAR

Sağ, sol ve orta menfez hattındaki açıklıklardan çıkan hava hızları Model 1, Model 2 ve Model 3 olarak incelenmiştir. Model 1'de, menfez geometrisi dikdörtgen ve çapı 50 mm olan hortum kullanılarak tasarlanmıştır ve klima çıkış bölümünde hava ayırma perdesi bulunmamaktadır. Model 2'de, menfez geometrisi dikdörtgen ve çapı 70 mm olan hortum kullanılacak şekilde tasarlanmıştır. Model 3'de menfez geometrisi daire ve çapı 70 mm olan hortum olacak şekilde hava çıkış menfezlerinin çapı 68 mm olarak tasarlanmıştır. Model 2 ve Model 3 için klima çıkış bölümünde hava ayırma perdesi bulunmaktadır. Şekil 2'de bulunan sağ menfez hattı analiz sonuçlarına bakıldığında, Model 2 ve Model 3 için klimaya yakın olan hava çıkış noktalarında akış hızlarının yaklaşık 4500 m/s ulaştığı ve Model 2'de dengesiz bir dağılım görünürken, Model 3'te bu hava çıkış noktalarındaki dağılımın daha dengeli olduğu görülmektedir.

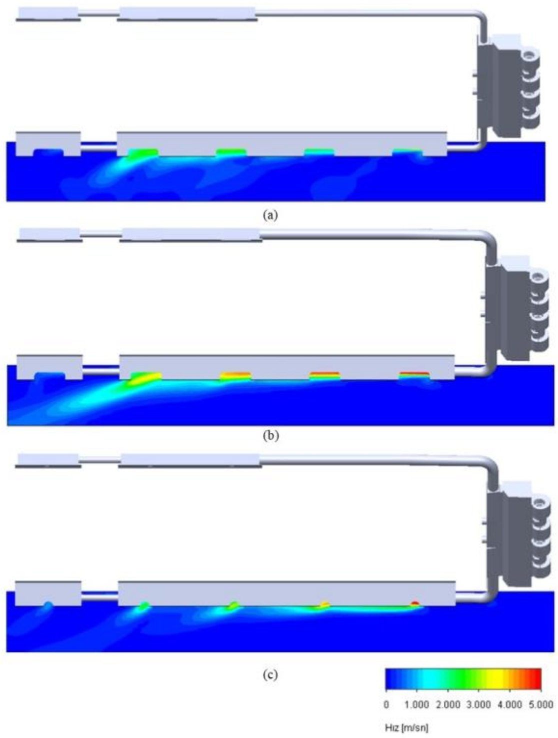

Şekil 2: Sağ menfez hattındaki (a) Menfez çapı 50mm, dikdörtgen, (b) Menfez çapı 70mm, dikdörtgen, (c) Menfez çapı 70mm, daire (68mm) menfez açıklıklarından çıkan hava hızları analizi

Sol menfez hattı analiz sonuçlarına göre, Şekil 3-a ve Şekil 3-b'ye bakıldığında boru çapının artırılmasıyla birlikte hava jetinin daha yüksek hız ve momentumla kabin içerisine iletildiği görülmektedir. Ancak, menfez boyutlarının büyük olması nedeniyle akış belirli bir yönde yoğunlaşarak ilerlemekte ve jet etkisi oluşturmakta, bu da lokal yüksek hız bölgelerine karşılık kabin genelinde dengesiz bir dağılıma neden olmaktadır. Menfezlerin dairesel formda ve uygun çapta (68 mm) tasarlanmasıyla birlikte (Şekil 3-c) hava akışının daha kontrollü ve dengeli bir şekilde dağıldığı gözlemlenmiştir. Yüksek hız bölgelerinin lokal olarak sınırlı kaldığı, akışın daha geniş bir alana yayıldığı ve hız gradyentlerinin azaldığı görülmektedir. Bu durum, kabin içerisinde daha homojen bir hava sirkülasyonu sağlandığını göstermektedir.

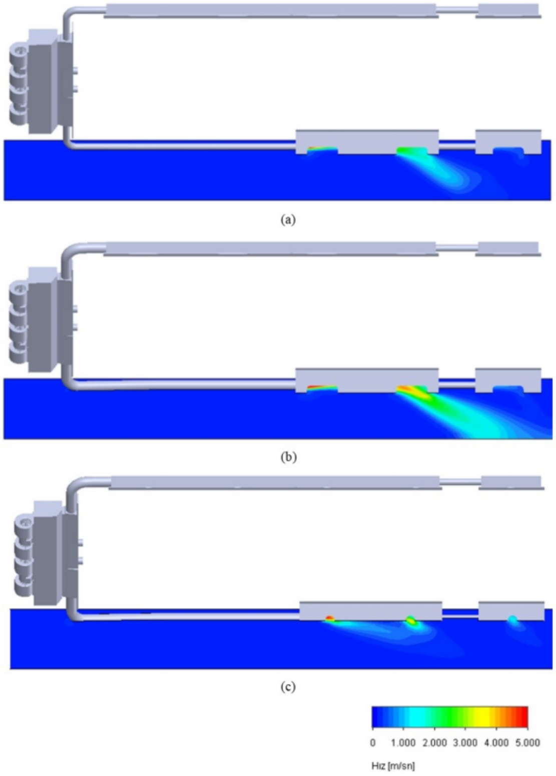

Şekil 3: Sol menfez hattındaki (a) Menfez çapı 50mm, dikdörtgen, (b) Menfez çapı 70mm, dikdörtgen, (c) Menfez çapı 70mm, daire (68mm) menfez açıklıklarından çıkan hava hızları analizi

Klima orta menfez hattında gerçekleştirilen analizde 3 model için de hava çıkış noktalarında, akış hızlarının en hızlı olan bölgeler olduğu Model 1'de hız seviyelerinin yaklaşık 4750 m/s hızlarında, akış boyunca ve keskin bir şekilde devam ettiği görülmektedir. Model 3'te diğerlerine göre daha homojen hız akışı gözlenmektedir.

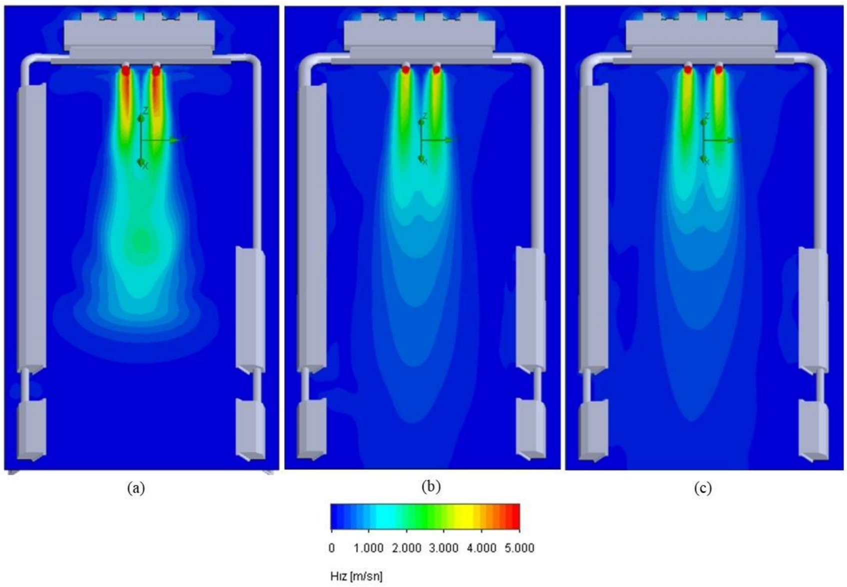

Şekil 4: Orta menfez hattındaki (a) Menfez çapı 50mm, dikdörtgen, (b) Menfez çapı 70mm, dikdörtgen, (c) Menfez çapı 70mm, daire (68mm) menfez açıklıklarından çıkan hava hızları analizi

4. TARTIŞMA

Gerçekleştirilen sayısal analizler sonucunda, farklı tasarım parametrelerinin araç içi hava dağılımı üzerinde belirleyici etkileri olduğu ortaya konmuştur. Üç farklı tasarım senaryosunun (Model 1, Model 2 ve Model 3) karşılaştırılmasıyla, havalandırma performansı açısından en uygun konfigürasyon belirlenmiştir.

1. modelde, kullanılan boru çapının yetersiz olduğu ve buna karşılık menfez boyutlarının gereğinden büyük tasarlandığı tespit edilmiştir. Bu durum, hava akışının menfezler arasında dengesiz dağılmasına ve bazı bölgelerde düşük hız değerlerinin oluşmasına neden olmuştur. 2. modelde ise boru çapı artırılarak akış kapasitesi iyileştirilmiş; ancak menfez boyutlarının hâlâ büyük olması nedeniyle hava hız dağılımında istenilen homojenlik sağlanamamıştır.

3. model tasarımında, boru çapının artırılması ile birlikte menfez geometrisi dairesel formda ve 68 mm çapında olacak şekilde optimize edilmiştir. Bu konfigürasyon sonucunda, menfezlerden çıkan hava hızlarının daha dengeli ve homojen bir şekilde dağıldığı gözlemlenmiştir. Ayrıca, akışın sistem genelinde daha kararlı ilerlediği ve hız farklılıklarının minimize edildiği belirlenmiştir.

Elde edilen bulgular, havalandırma sistemlerinde boru çapı ve menfez geometrisinin birlikte optimize edilmesinin, hava dağılım performansı üzerinde doğrudan etkili olduğunu göstermektedir. Bu doğrultuda, menfez geometrisinin dairesel olması, önceki konfigürasyonlara kıyasla daha etkin bir hava sirkülasyonu sağlayarak araç içi konforun artırılması açısından en uygun çözüm olarak değerlendirilmiştir.

STATEMENTS AND DECLARATIONS

Supplementary Material

All supplementary or supporting information provided by the authors will be published online alongside the main article. When such material is available, it will also be indicated here along with a link to the pdf for downloading.

Acknowledgements

Projede bizlerden desteklerini esirgemeyen OTM Plastik Otomotiv Yan Sanayi ve Ticaret Ltd. Şti. yöneticilerimiz ve çalışma arkadaşlarımıza, ortak çalışma imkânı bulduğumuz Yılkar Klima yetkililerine teşekkürlerimizi borç biliriz.

Author Contributions

Provide a detailed account of each author’s contributions to the research and writing of the paper, following the CRediT (Contributor Roles Taxonomy) format. https://credit.niso.org/

Conflicts of Interest

Disclose any actual or potential conflicts of interest that could influence the research. If there are no conflicts, state this explicitly.

Data, Code & Protocol Availability

Provide information on the availability of data, code, and protocols. Specify where these materials can be accessed, such as public repositories or upon request. Assigned DOI or other identification numbers, links and any conditions that may be present in order to obtain access should be included. This information should also be included in the references and cited in the text.

Funding Received

List all sources of funding or financial support received for the research. Include grant numbers and the names of funding organizations.

ORCID IDs

Ümmet Ayyıldız https://orcid.org/0000-0001-9340-0115
Songül Kılınç https://orcid.org/0000-0003-1035-477X
Kadir Güyen https://orcid.org/0009-0005-2674-6200

REFERENCES

1. T. B. Chang, J. J. Sheu, J. W. Huang, Y. S. Lin, and C. C. Chang, "Development of a CFD model for simulating vehicle cabin indoor air quality," Transp. Res. Part D Transp. Environ., vol. 62, pp. 433–440, 2018.
2. P. O. Fanger, Thermal Comfort: Analysis and Applications in Environmental Engineering. Copenhagen, Denmark: Danish Technical Press, 1970.
3. M. Vaughn, "ASHRAE research report: 2020–2021," ASHRAE J., vol. 63, no. 10, pp. 73–87, 2021.
4. T. B. Chang, J. J. Sheu, J. W. Huang, Y. S. Lin, and C. C. Chang, "Development of a CFD model for simulating vehicle cabin indoor air quality," Transp. Res. Part D Transp. Environ., vol. 62, pp. 433–440, 2018.
5. X. B. Xu, X. K. Chen, and J. Y. Xiong, "Air quality inside motor vehicles' cabins: A review," 2018.
6. O. A. Seppänen and W. Fisk, "Some quantitative relations between indoor environmental quality and work performance or health," HVAC&R Res., vol. 12, no. 4, pp. 957–973, 2006.
7. T. B. Chang, Y. S. Lin, and Y. T. Hsu, "CFD simulations of effects of recirculation mode and fresh air mode on vehicle cabin indoor air quality," Atmos. Environ., vol. 293, art. 119473, 2023.
8. S. Pawar, U. R. Gade, A. Dixit, S. B. Tadigadapa, and S. Jaybhay, "Evaluation of cabin comfort in air conditioned buses using CFD," in Proc. SAE 2014 World Congress & Exhibition, Apr. 2014.
9. B. Pirouz, D. Mazzeo, S. A. Palermo, S. N. Naghib, M. Turco, and P. Piro, "CFD investigation of vehicle's ventilation systems and analysis of ACH in typical airplanes, cars, and buses," Sustainability, vol. 13, no. 12, art. 6799, 2021.
10. W. P. Jones and B. E. Launder, "The prediction of laminarization with a two-equation model of turbulence," Int. J. Heat Mass Transf., vol. 15, no. 2, pp. 301–314, 1972.

Aintelia Science Notes

ASNJ • BAUDER PRESS

Research Article

From Unstructured Documents to Intelligent Insights: An End-to-End AI Pipeline for Global Tax Compliance

Muhammed Şara[1,*], Ahmet Ak[2], Ayhan Boyacıoğlu[3], Yunus Taştutan[4]

1, 2, 3, 4 Sovos/F.I.T. R&D Center, İstanbul, Türkiye

Correspondence to:
Muhammed Şara –
muhammed.sara@sovos.com
+90 539 714 6546

How to Cite:
Actual Citation as taken from website

RECEIVED: 28/04/2026
ACCEPTED: 08/05/2026
PUBLISHED: 30/06/2026

ABSTRACT

Over 60 countries now mandate electronic invoicing, and this number has since exceeded 100 countries. Turkey is among the earliest adopters, with the Turkish Revenue Administration (GİB) generating more than 2 billion documents annually. For enterprises operating across multiple jurisdictions, meeting these obligations creates serious operational and legal challenges that become increasingly difficult to manage as transaction volumes increase. Traditional rule-based approaches were not built for this scale; they struggle with heterogeneous input formats and cannot easily absorb changes in jurisdiction-specific tax rules. This study presents an end-to-end artificial intelligence pipeline that addresses these challenges by transforming unstructured invoice documents (PDFs, images, and CSV files) into actionable compliance insights within a single, unified architecture. The pipeline integrates three tightly coupled components. The Smart Input Module uses a competitive ensemble of large multimodal models: Google Gemini Flash, Amazon Nova Lite, and OpenAI GPT-4.1 to extract tax-relevant fields from diverse document formats, achieving 92% overall extraction accuracy and 98% accuracy on legally critical fields, such as tax identification numbers and monetary amounts. The Cloud Processing Layer introduces a domain-specific XSLT deduplication technique that exploits a structural regularity unique to Turkish e-invoices: embedded rendering stylesheets that are nearly identical across documents from the same taxpayer. By replacing duplicate stylesheets with compact SHA-256 hash references while reinserting exact original bytes during reconstruction to preserve digital signature integrity, the system achieves 90% compression on document content, contributing to a 63% reduction in total storage footprint and extending the infrastructure runway from 18 months to over five years. An event-driven architecture built on RabbitMQ and Kubernetes autoscaling raises the peak throughput from 32 to 200 transactions per second, a 6.25× improvement. Redis caching further reduced the taxpayer lookup latency from 10 ms to 0.9 µs. The Sovi Intelligence Engine completes the pipeline by enabling natural language querying of processed tax data in Turkish, English, German, French, and Spanish. Based on an agentic architecture, Sovi decomposes each query into sub-steps: intent interpretation, schema mapping, and SQL generation, guided by a retrieval-augmented generation workflow that maps domain terminology to database columns. In the evaluation, the system achieved a 94% valid SQL generation rate and 82% semantic accuracy, with a mean response latency of 3.2 s and a user satisfaction score of 4.1 out of 5. Running in production today, the pipeline demonstrates that fully automated, AI-driven tax compliance is not a future aspiration but a current reality in Turkey.

KEYWORDS

Document AI, Tax Compliance, Large Language Models, Natural Language Processing, Electronic Invoicing

1. Introduction

Over 60 countries now mandate electronic invoicing, and this number has since exceeded 100 countries [1]. Turkey is among the earliest adopters; the Turkish Revenue Administration (GİB) requires all businesses above certain revenue thresholds to issue invoices electronically through its platform, generating more than 2 billion documents annually. For enterprises operating across multiple jurisdictions, meeting these obligations creates serious operational and legal challenges that become increasingly difficult to manage as transaction volumes increase.

Traditional approaches, such as manual data entry combined with rule-based validation, were not built for this scale. They struggle with the range of input formats encountered in practice, from scanned paper invoices to structured XML, and cannot easily absorb changes in jurisdiction-specific tax rules. Recent developments in document AI and large language models (LLMs) suggest a different path, where the extraction, validation, and analysis of tax documents can be handled with far less human intervention [2,3,4,5].

This paper addresses this fragmentation by presenting a unified pipeline, deployed in production at Sovos, that spans the full compliance lifecycle—from raw document ingestion to natural language querying of processed tax records—integrating extraction, storage, and analytics within a single architecture.

2. Materials and Methods

The system consists of three modules: Smart Input, Cloud Processing, and Sovi Intelligence Engine, connected through a RabbitMQ event bus (see Figure 1). The evaluation uses a production dataset of 5,000 invoices drawn from approximately 1,000 unique recipient taxpayers and 50-100 distinct issuing companies, with the ground truth established through manual verification followed by automated validation tools.

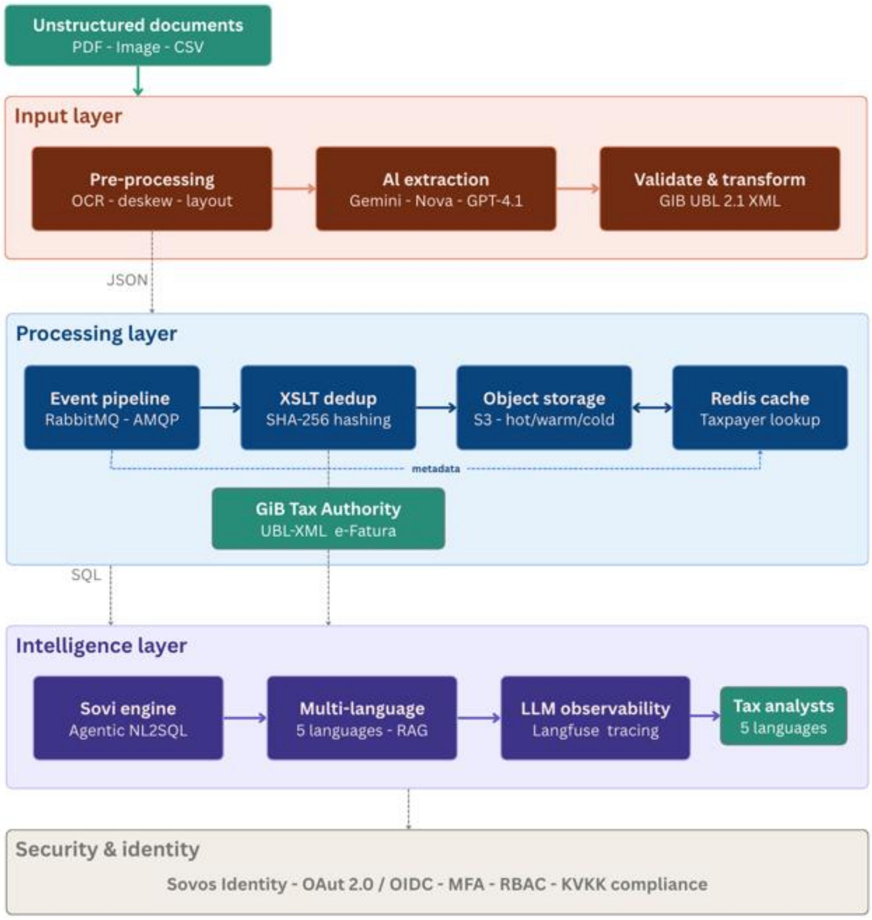

Figure 1: *End-to-end AI pipeline for tax compliance: Input Layer (orange), Processing Layer (blue), Intelligence Layer (purple), and Security Layer (gray).*

Smart Input Module

The Smart Input module transforms unstructured documents (PDF, JPEG/PNG, CSV) into GİB-compliant UBL 2.1 XML format. A format detection layer directs each document to the corresponding processing path based on the format and quality metrics. For image-based inputs, a three-stage pre-processing sequence applies deskewing, noise reduction, and contrast normalization before the layout analysis segments the document into header, line-item, and summary regions.

We evaluated three model providers on 5,000 production invoices: Google Gemini Flash, Amazon Nova Lite, and OpenAI GPT-4.1. Each extracted JSON output is then validated through check-digit verification of tax IDs (VKN/TCKN), cross-reference against the GİB taxpayer registry, and semantic consistency checks against Turkish VAT rules.

Cloud Processing Layer

The processing layer was built around an event-driven architecture using RabbitMQ (AMQP). Because the stages are decoupled, each stage can be scaled independently, which is a critical property during month-end demand spikes when transaction volumes rise sharply and unpredictably. Kubernetes Horizontal Pod Autoscaling adjusts the worker count from 4 to 24 replicas in response to the queue depth and CPU utilization metrics.

A significant optimization opportunity arose from the XSLT stylesheets embedded in Turkish e-invoices. These stylesheets allow recipients to view invoices in a browser without specialized software, but they are nearly identical across documents from the same taxpayer, a structural regularity that is invisible to general-purpose compression algorithms. Our content-addressable storage strategy computes the SHA-256 hash of each stylesheet and replaces the duplicates with a compact reference pointer, storing the unique stylesheets separately for reconstruction. Reconstruction reinserts the exact original bytes, preserving the byte-level digital signature integrity, which was validated using the official GİB e-Fatura Görüntüleyici tool. Document metadata is persisted to PostgreSQL via the Outbox Pattern and replicated asynchronously to S3-compatible object storage with hot/warm/cold tiering (0–30, 30–365, 365–3,650 days).

Sovi Intelligence Engine

The Sovi Intelligence Engine provides natural language analytics for processed tax data. Rather than a single-step translation from query to SQL, Sovi decomposes each request into sub-steps: first interpreting the user's intent, then mapping it to the relevant schema elements, and finally generating and executing the SQL, following an established query decomposition approach [6, 7]. A Retrieval-Augmented Generation (RAG) workflow guides this categorization step, supplying a domain vocabulary that maps Turkish tax terminology – KDV (VAT), mükellef (taxpayer), stopaj (withholding) – to the corresponding database columns [8]. The system accepts queries in Turkish, English, German, French, and Spanish, and all LLM interactions are monitored via Langfuse for trace logging, cost-tracking, and quality metrics [9].

3. Result

Smart Input Evaluation

As Table 1 shows, all three providers hit 98% accuracy on critical fields – the ones that determine legal validity – although their overall scores and costs diverge considerably. Gemini Flash leads on overall accuracy at 92%, while Nova Lite offers the lowest cost at $0.02 per document, compared to $0.055 for GPT-4.1. Line-item extraction was the most challenging task, reaching only 89.3% because of merged cells and inconsistent column ordering across templates. Interestingly, errors showed no preference for any particular industry; they clustered around documents with unusual layouts regardless of the sector.

Table 1: *AI Model Comparison for Invoice Extraction*

Metric	Gemini Flash	Nova Lite	GPT-4.1
Overall Accuracy	92%	90%	89%
Critical Field Accuracy	98%	98%	98%
Avg. Processing Time	4.5 s	5.2 s	4.2 s
Cost per 1,000 docs (API)	$40	$20	$55

Processing Layer Evaluation

Migrating from batch processing to the event-driven architecture increased peak throughput from 32 to 200 TPS, a 6.25× improvement. Scaling is near-linear up to 16 workers, with diminishing returns beyond 20 workers attributable to HTTP server and CPU resource boundaries rather than database lock contention, indicating that the bottleneck is computational rather than state-dependent, and is addressable through standard horizontal scaling.

Table 2: *Storage Optimisation Results*

Metric	Before	After
Total data volume	150 TB	55 TB
Monthly growth rate	3 TB/month	650 GB/month
Full backup duration	4 days	1.5 days
Query latency (taxpayer lookup)	10 ms	0.9 μs

XSLT deduplication alone achieves a 90% size reduction in document content, outperforming general-purpose XML compression, which yielded only a 4× ratio on the same corpus. Combined with tiered storage and metadata optimization, the total volume decreased from 150 to 55 TB. Monthly growth dropped by 78%, extending the infrastructure runway from 18 months to over five years. Redis caching reduced taxpayer lookup latency by more than four orders of magnitude, from 10 ms to 0.9 μs.

Figure 2 illustrates the scaling behavior of the optimized system relative to the static baseline.

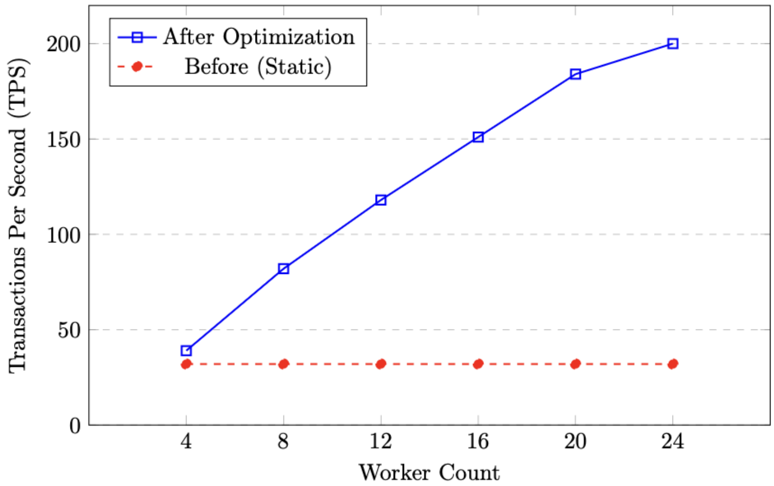

Figure 2: *System throughput scaling with the worker count. The optimised system shows near-linear scaling up to 16 workers.*

Sovi Intelligence Evaluation

Table 3 reports the Sovi performance metrics based on the model generation time as the primary latency measure, with user satisfaction derived from the Net Promoter Score responses normalized to a 5-point scale.

Table 3: *Natural Language Query Evaluation*

Metric	Value
Valid SQL syntax generation rate	94%
SQL semantic accuracy	82%
Avg. response latency (model generation)	3.2 s
User satisfaction (1–5, NPS-derived)	4.1

The 82% semantic accuracy is comparable with the performance of leading NL2SQL systems on domain-specific benchmarks [10]. The 12-point gap between syntactic validity (94%) and semantic accuracy (82%) reflects ambiguous GROUP BY selections in aggregation queries and off-by-one boundary errors in temporal comparisons. English queries (80% of the volume) achieved the highest success rate at 88%, followed by Turkish (15%) at 81%, while German/French/Other (5%) reached 61% likely reflecting the smaller test set for those languages rather than an inherent capability gap, though further evaluation is needed to confirm this.

4. Discussion and Conclusion

The most notable finding is that model selection has little bearing on legally critical fields: all three providers achieved 98% accuracy on tax IDs and monetary amounts. Differences emerge on less structured content such as line items, where cost-accuracy trade-offs become operationally significant. The second finding concerns storage: domain-specific XSLT deduplication achieved 10× compression on the same data that general-purpose algorithms compressed by only 4×, demonstrating that domain-specific regulatory knowledge can unlock optimisations that general-purpose compression tools cannot achieve. Finally, the move to an event-driven architecture was not a marginal improvement; it transformed a system that topped out at 32 TPS regardless of added resources into one that scaled linearly with worker count up to 200 TPS.

An earlier project, the Indirect Tax Analytics (ITA) Framework, spent 18 months attempting to map data from over 30 global tax systems into a single canonical schema before the effort was discontinued. The maintenance burden grew faster than the value delivered: each new country or document type added not only new mappings but also new conflicts with existing ones. The Sovi engine takes the opposite approach, providing natural language abstraction over heterogeneous data stores at query time, rather than forcing schema homogeneity upfront. The result was a system that reached production in eight months and has remained stable since.

This production deployment demonstrates that end-to-end AI-driven tax compliance is technically feasible and operationally viable at enterprise scale. Priority directions for future work include proactive anomaly detection to shift the system from reactive audit support toward pre-emptive risk management, and multi-jurisdictional expansion as the EU VAT in the Digital Age (ViDA) initiative extends comparable mandates to European markets.

STATEMENTS AND DECLARATIONS

Supplementary Material

No supplementary material accompanies this article.

Acknowledgements

The authors thank the engineering team at Sovos Turkey for their contributions to the system development.

Author Contributions

M. Şara: Conceptualization, Methodology, Software, Investigation, Writing – Original Draft, Writing – Review & Editing. A. Ak: Software, Validation, Data Curation. A. Boyacıoğlu: Software, Investigation, Visualization. Y. Taştutan: Methodology, Formal Analysis, Writing – Review & Editing.

Conflicts of Interest

The authors declare that there is no conflict of interest. The authors are affiliated with Sovos/F.I.T. R&D Center, whose production system is described in this study.

Data, Code & Protocol Availability

The invoice dataset used in this study contains proprietary and confidential taxpayer information and cannot be publicly shared. Aggregated results and methodology details are available from the corresponding author upon reasonable request.

Funding Received

This research did not receive any specific grant from funding agencies in the public, commercial, or not-for-profit sectors.

ORCID IDs

Muhammed Şara https://orcid.org/0000-0002-8353-3544
Ahmet Ak https://orcid.org/0009-0001-2660-860X
Ayhan Boyacıoğlu https://orcid.org/0009-0001-2906-2526
Yunus Taştutan https://orcid.org/0009-0001-1262-1838

REFERENCES

1. Billentis, "E-invoicing/e-billing: Digitisation & automation," Market Rep., 2023. [Online]. Available: https://www.billentis.com/
2. Y. Xu, M. Li, L. Cui, S. Huang, F. Wei, and M. Zhou, "LayoutLM: Pre-training of text and layout for document image understanding," in Proc. 26th ACM SIGKDD Conf. Knowl. Discov. Data Min., 2020, pp. 1192–1200, doi: 10.1145/3394486.3403172.
3. Y. Huang, T. Lv, L. Cui, Y. Lu, and F. Wei, "LayoutLMv3: Pre-training for document AI with unified text and image masking," in Proc. 30th ACM Int. Conf. Multimedia, 2022, pp. 4083–4091, doi: 10.1145/3503161.3548112.
4. D. Wang, N. Ravi, C. Arber, S. Bhatia, and A. Chakravarthi, "DocLLM: A layout-aware generative language model for multimodal document understanding," in Proc. ACL, 2024, pp. 2551–2568.
5. L. Li, Y. Zhang, and L. Chen, "A survey on large language models for recommendation," World Wide Web, vol. 27, no. 5, pp. 1–35, 2024, doi: 10.1007/s11280-024-01291-2.
6. A. Plaat, T. Muller, and J. van den Herik, "Agentic large language models: A survey," J. Artif. Intell. Res., vol. 82, pp. 345–412, 2025, doi: 10.1613/jair.1.16853.
7. M. Pourreza and D. Rafiei, "DIN-SQL: Decomposed in-context learning of text-to-SQL with self-correction," in Adv. Neural Inf. Process. Syst., vol. 36, 2023.
8. A. Plaat, A. Wong, and J. van den Herik, "Multi-step reasoning with large language models: A survey," ACM Comput. Surv., vol. 57, no. 3, pp. 1–38, 2024, doi: 10.1145/3717843.
9. Langfuse GmbH, "Langfuse: Open source LLM engineering platform," Software documentation, 2023. [Online]. Available: https://langfuse.com/
10. J. Li et al., "Can LLM already serve as a database interface? A big bench for large-scale database grounded text-to-SQL," in Adv. Neural Inf. Process. Syst., vol. 37, 2024.

Aintelia Science Notes

ASNJ • BAUDER PRESS

Technical Note

An Investigation of the Effects of Cationic Conditioning Systems on Hair Combability and Sensory Performance

Katyonik Kondisyoner Sistemlerin Saçta Taranabilirlik ve Duyusal Performans Üzerine Etkilerinin İncelenmesi

Aslı Eren Yüksel[1,*]

1 Kale Care Chemicals, İstanbul, Türkiye

Correspondence to:
Aslı Eren Yüksel – asli.yuksel@kalecare.com

How to Cite:
Actual Citation as taken from website

RECEIVED: 30/04/206
ACCEPTED: 03/05/2026
PUBLISHED: 30/06/2026

ABSTRACT

In this study, the surface interactions of cationic surfactant-based conditioning systems on hair fibers and the resulting performance outcomes were comprehensively evaluated. The negatively charged surface characteristics of hair fibers, particularly after washing, facilitate the adsorption of cationic agents onto the hair surface via electrostatic attraction. As a result of this adsorption mechanism, a low-friction film layer is formed on the hair surface, reducing inter-fiber interaction forces and improving combability performance. Within the scope of the study, formulations containing cationic conditioning systems were comparatively evaluated against reference systems, and all formulations were standardized based on an equivalent active matter concentration of 2%. Wet and dry combing performance was assessed using a texture analyzer by measuring combing force values. Sensory evaluations were conducted by trained panelists under a blind test protocol and scored using a multi-parameter approach. The findings demonstrated that cationic systems form a homogeneous and stable film layer on the hair surface, significantly reducing the coefficient of friction and markedly improving both wet and dry combability. Furthermore, a strong correlation was observed between sensory evaluation results and instrumental measurements. In conclusion, cationic surfactant-based conditioning systems provide high-performance and sensorially optimized solutions in modern hair care formulations.

KEYWORDS

hair, conditioner, hair cream, hair fiber, hair combing test

ÖZET

Bu çalışmada, katyonik yüzey aktif maddelere dayalı kondisyoner sistemlerin saç lifi üzerindeki yüzey etkileşimleri ve buna bağlı performans çıktıları kapsamlı olarak değerlendirilmiştir. Saç lifinin özellikle yıkama sonrasında negatif yüklü bir yüzey karakteri göstermesi, katyonik ajanların elektrostatik çekim yoluyla saç yüzeyine adsorbe olmasını mümkün kılmaktadır. Bu adsorpsiyon mekanizması sonucunda saç yüzeyinde düşük sürtünmeli bir film tabakası oluşmakta, lifler arası etkileşim kuvvetleri azalmakta ve taranabilirlik performansı iyileşmektedir. Çalışma kapsamında, katyonik kondisyoner sistemler içeren formülasyonlar referans sistemler ile karşılaştırmalı olarak incelenmiş; tüm sistemler eşdeğer aktif madde konsantrasyonu (%2) esas alınarak standardize edilmiştir. Islak ve kuru tarama performansı, tekstür analiz cihazı kullanılarak tarama kuvveti (combing force) ölçümleri üzerinden değerlendirilmiştir. Duyusal analizler, eğitimli panelistler tarafından kör test protokolü çerçevesinde gerçekleştirilmiş ve çok parametreli bir yaklaşım ile skorlanmıştır. Elde edilen bulgular, katyonik sistemlerin saç yüzeyinde homojen ve stabil bir film tabakası oluşturarak sürtünme katsayısını anlamlı düzeyde azalttığını ve hem ıslak hem kuru taranabilirliği belirgin şekilde iyileştirdiğini ortaya koymuştur. Ayrıca duyusal değerlendirmeler ile enstrümantal ölçümler arasında yüksek düzeyde korelasyon saptanmıştır. Sonuç olarak, katyonik yüzey aktif maddelere dayalı kondisyoner sistemlerin, saç bakım formülasyonlarında yüksek performanslı ve duyusal açıdan optimize edilmiş çözümler sunduğu ortaya konmuştur.

Anahtar Kelimeler: *saç, kondisyoner, saç kremi, saç lifi, saç tarama testi*

1. Giriş

Saç, kıl folikülü tarafından sentezlenen; proteinler, lipitler, su ve pigmentler gibi minör bileşenlerden oluşan lifsi yapıda bir kompozit biyomateryaldir. Saçın yapısal bütünlüğü ve mekanik dayanımı büyük ölçüde protein içeriğine bağlı olup, proteinler toplam saç kütlesinin yaklaşık %65–95'ini oluşturmaktadır.

Saç bakım ürünleri, saç lifinin mekanik bütünlüğünü korumak, yüzey hasarını minimize etmek ve taranabilirliği iyileştirmek amacıyla geliştirilmektedir. Bu kapsamda, ıslak ve kuru taranabilirlik parametreleri, ürün performansının değerlendirilmesinde temel göstergeler arasında yer almaktadır.

Kondisyoner ajanlar, saç lif yüzeyine adsorbe olarak lifler arası sürtünmeyi ve elektrostatik yük birikimini azaltmakta; bu sayede saçın daha kolay taranabilir olmasına katkı sağlamaktadır.

2. Materyal ve Yöntem

Tablo 1: *Kullanılan Malzeme*

Malzeme Adı	Firma Adı
Cetearyl Alcohol	SASOL
Behentrimonium Methosulfate	SYENSQO

Saçın taranabilirlik performansı, tekstür analiz cihazı kullanılarak ölçülen tarama kuvveti değerleri üzerinden değerlendirilmiştir. Standartlaştırılmış saç tutamları yıkanmış, kondisyoner uygulanmış ve durulanmıştır. Saç tutamı cihazın tutucu sistemine sabitlenmiş ve standart bir tarak ile sabit hızda taranmıştır. Tarama sırasında oluşan direnç kuvveti ölçülmüştür. Testler hem ıslak hem kuru saç üzerinde gerçekleştirilmiş ve elde edilen kuvvet değerleri karşılaştırılarak analiz edilmiştir.

3. Sonuçlar

Elde edilen bulgular, katyonik yüzey aktif maddelerin saç yapısı üzerinde yüksek etkinliğe sahip bir kondisyoner ajan olarak davrandığını ve saç yüzeyinde homojen ve stabil bir film tabakası oluşturarak sürtünmeyi anlamlı düzeyde azalttığını açıkça ortaya koymaktadır.

Bileşenin katyonik karakteri sayesinde, saçın negatif yüklü bölgelerine güçlü elektrostatik etkileşimlerle bağlandığı; bu adsorpsiyon mekanizmasının kütikül yapısının yeniden düzenlenmesine katkı sağlayarak hem ıslak hem de kuru taranabilirliği belirgin şekilde iyileştirdiği değerlendirilmektedir.

Duyusal analiz bulguları ile enstrümantal ölçümler arasında yüksek düzeyde korelasyon gözlenmiş olup, katyonik yüzey aktif maddelerin saç üzerinde dengeli bir yumuşaklık ve belirgin kayganlık sağlarken, ağırlaşma hissi oluşturmadan optimum kondisyoner performans sunduğu doğrulanmıştır.

Sonuç olarak, katyonik yüzey aktif maddelerin modern saç bakım formülasyonlarında yalnızca etkili bir kondisyoner ajan olarak değil, aynı zamanda üstün duyusal profil sağlayan, yüksek performanslı ve formülasyon açısından rekabetçi bir bileşen olarak konumlandırılabileceği ortaya konmuştur.

STATEMENTS AND DECLARATIONS

Supplementary Material

No supplementary material accompanies this article.

Acknowledgements

The author would like to thank Kale Care Chemicals for providing the raw materials, texture analysis instrumentation, and sensory panel coordination used throughout this study.

Author Contributions

A. Eren Yüksel: Conceptualization, Methodology, Formulation Development, Investigation, Formal Analysis, Writing – Original Draft, Writing – Review & Editing.

Conflicts of Interest

The author declares that there is no conflict of interest. The author is affiliated with Kale Care Chemicals, which manufactures cosmetic raw materials referenced in this study.

Data, Code & Protocol Availability

The data supporting the findings of this study are available from the corresponding author upon reasonable request.

Funding Received

This research did not receive any specific grant from funding agencies in the public, commercial, or not-for-profit sectors.

ORCID IDs

Aslı Eren Yüksel https://orcid.org/0009-0006-2656-0374

REFERENCES

1. C. Fernandes, B. Medronho, L. Alves, and M. G. Rasteiro, "On hair care physicochemistry: From structure and degradation to novel biobased conditioning agents," Polymers, vol. 15, no. 3, art. 608, 2023, doi: 10.3390/polym15030608.
2. C. R. Robbins, "Chemical composition of different hair types," in Chemical and Physical Behavior of Human Hair, New York, NY, USA: Springer, 2011, pp. 105–176, doi: 10.1007/978-3-642-25611-0_2.
3. H. A. Benson, M. S. Roberts, V. R. Leite-Silva, and K. A. Walters, Eds., Cosmetic Formulation: Principles and Practice. Boca Raton, FL, USA: CRC Press, 2019, doi: 10.1201/9780429190674.

Aintelia Science Notes

ASNJ • BAUDER PRESS

Technical Note

The Multifunctional Effects of Niacinamide, Sodium Hyaluronate, and Hydrolyzed Collagen

Niasinamid, Sodyum Hiyalüronat ve Hidrolize Kolajenin Multifonksiyonel Etkileri

Tuba Güneş[1]

1 Kale Care Chemicals Kimyevi Maddeler A.Ş., İstanbul, Türkiye

Correspondence to:
Tuba Güneş –
tuba.gunes@kalecare.com

How to Cite:
Actual Citation as taken from website

RECEIVED: 30/04/2026
ACCEPTED: 08/05/2026
PUBLISHED: 30/06/2026

ABSTRACT

Skin aging is characterized by moisture loss, a decrease in collagen, and a slowing of cellular renewal. During this process, structural and functional changes occur in the epidermis, dermis, and hypodermis layers. In this study, a multifunctional active complex containing hyaluronic acid, niacinamide, and hydrolyzed collagen was developed and incorporated into a facial serum at a 5% concentration. The formulation's efficacy was evaluated over a 4-week period on 20 female volunteers aged 25–39. Following the application of the serum twice daily, an increase in skin hydration and smoothness, as well as a reduction in dryness and the appearance of fine lines, was observed. The findings indicate that the developed active complex provides skin brightening and is effective in reducing signs of aging.

Keywords: *Niacinamide, Sodium Hyaluronate, Collagen, Anti-Aging*

ÖZET

Cilt yaşlanması; nem kaybı, kolajen azalması ve hücresel yenilenmenin yavaşlaması ile karakterizedir. Bu süreçte epidermis, dermis ve hipodermis katmanlarında yapısal ve fonksiyonel değişimler meydana gelir. Bu çalışmada, hiyalüronik asit, niasinamid ve hidrolize kolajen içeren çok fonksiyonlu bir aktif kompleks geliştirilmiş ve %5 oranında yüz serumuna entegre edilmiştir. Formülasyonun etkinliği, 25–39 yaş aralığındaki 20 kadın gönüllü üzerinde 4 hafta boyunca değerlendirilmiştir. Günde iki kez uygulanan serumun kullanım sonucunda, cilt neminde ve pürüzsüzlüğünde artış, kuruluk ve ince kırışıklık görünümünde ise azalma gözlemlenmiştir. Bulgular, geliştirilen aktif kompleksin cilt yüzeyinde aydınlanma sağladığını ve yaşlanma belirtilerinin azaltılmasında etkili olduğunu göstermektedir.

Anahtar Kelimeler *Niasinamid, Sodyum Hiyalüronat, Kolajen, Yaşlanma Karşıtı*

1. Giriş

Cilt dokusu, yaşlanma süreci ve çevresel faktörlerin etkisiyle zaman içerisinde yenilenme kapasitesinde ve elastikiyetinde azalma göstermektedir. Bu sürecin temelinde, hücresel anabolik aktivitenin yavaşlaması ile ultraviyole radyasyon, hava kirliliği ve uygunsuz cilt bakım alışkanlıkları gibi dış etkenlerin cilt üzerinde oluşturduğu kümülatif hasar yer almaktadır. Söz konusu değişimlerin önlenmesi veya etkilerinin azaltılması amacıyla çeşitli kozmetik aktif bileşenlerden yararlanılmaktadır. Bu çalışmada, farklı etki mekanizmalarına sahip hiyalüronik asit, niasinamid ve hidrolize kolajen bir araya getirilerek çok fonksiyonlu bir aktif kompleks geliştirilmiş ve bu kompleksin kişisel bakım ürünlerinde cilt dokusu üzerindeki performansı değerlendirilmiştir.

2. Materyal ve Yöntem

Tablo 1: *Deneme Data*

Bileşen	**Tedarikçi**
Niacinamide	JUBILANT INGREVIA
Sodium Hyaluronate 10 KDa	AMHWA BIOPHARM
Sodium Hyaluronate 300 KDa	AMHWA BIOPHARM
Sodium Hyaluronate 1000 KDa	AMHWA BIOPHARM
Hydrolyzed Collagen	VISCOFAN

Bu çalışmada, hiyalüronik asit, niasinamid ve hidrolize kolajen içeren çok fonksiyonlu bir aktif kompleks geliştirilmiştir. Formülasyon tasarımında, söz konusu aktif bileşenlerin nemlendirme, cilt bariyerini destekleme ve yaşlanma karşıtı etkileri dikkate alınmıştır. Geliştirilen aktif kompleks, yüz serumu formülasyonuna %5 (w/w) oranında dahil edilmiştir.

Formülasyonun etkinliği, 25–39 yaş aralığında yer alan 20 sağlıklı kadın gönüllü üzerinde değerlendirilmiştir. Çalışma kapsamında gönüllülerden, serumu dört hafta boyunca günde iki kez (sabah ve akşam), temizlenmiş yüz bölgesine uygulamaları istenmiştir. Her uygulamada yaklaşık 2 mL ürün kullanılmış; serum, parmak uçları yardımıyla nazik ve dairesel hareketlerle cilt yüzeyine homojen şekilde uygulanmıştır.

Ürünün cilt üzerindeki etkileri, çalışma süresince gönüllülerden elde edilen öznel değerlendirmeler doğrultusunda analiz edilmiştir. Değerlendirme kriterleri arasında cilt nem düzeyi, pürüzsüzlük, dolgunluk, kuruluk seviyesi ve kırışıklık görünümündeki değişimler yer almıştır. Elde edilen veriler, geliştirilen formülasyonun cilt görünümü ve cilt hissi üzerindeki etkilerini kapsamlı bir şekilde ortaya koymak amacıyla değerlendirilmiştir.

3. Sonuçlar

Üç aktifin kombinasyonu cilt üzerinde sinerjik etki sağlar.

Nemlendirme + bariyer + yaşlanma karşıtı özellikler birlikte optimize edilir.

Yüksek katma değerli kozmetik ürün geliştirme imkânı sunar.

Girdilerin kombine halde kullanımı operasyonel anlamda iş yükünü azaltırken, proses süresinin kısaltılmasına destek olur.

STATEMENTS AND DECLARATIONS

Supplementary Material

No supplementary material accompanies this article.

Acknowledgements

The author would like to thank Kale Care Chemicals Kimyevi Maddeler A.Ş. for providing the raw materials, laboratory infrastructure, and volunteer panel coordination used throughout this study.

Author Contributions

T. Güneş: Conceptualization, Methodology, Formulation Development, Investigation, Formal Analysis, Writing – Original Draft, Writing – Review & Editing.

Conflicts of Interest

The author declares that there is no conflict of interest. The author is affiliated with Kale Care Chemicals Kimyevi Maddeler A.Ş., which manufactures cosmetic raw materials referenced in this study.

Data, Code & Protocol Availability

The data supporting the findings of this study are available from the corresponding author upon reasonable request.

Funding Received

This research did not receive any specific grant from funding agencies in the public, commercial, or not-for-profit sectors.

ORCID IDs

Tuba Güneş https://orcid.org/0009-0007-9161-7290

REFERENCES

1. V. Nobile, D. Buonocore, A. Michelotti, and F. Marzatico, "Anti-aging and filling efficacy of six types hyaluronic acid based dermo-cosmetic treatment: Double blind, randomized clinical trial of efficacy and safety," J. Cosmet. Dermatol., vol. 13, no. 4, pp. 277–287, 2014, doi: 10.1111/jocd.12120.
2. H. Al-Atif, "Collagen supplements for aging and wrinkles: A paradigm shift in the field of dermatology and cosmetics," Dermatol. Pract. Concept., vol. 12, no. 1, art. e2022018, 2022, doi: 10.5826/dpc.1201a18.
3. E. Arca, M. Cayirli, E. Koc, and Z. Kurumlu, "Evaluation of efficacy and safety of niacinamide gel in the treatment of mild to moderate acne," Gulhane Med. J., vol. 55, no. 3, p. 167, 2013, doi: 10.5455/gulhane.22956.